nature portfolio

https://doi.org/10.1038/s41586-025-09673-w

Supplementary information

Slipknot-gauged mechanical transmission and robotic operation

In the format provided by the authors and unedited

Slipknot gauged mechanical transmission and robotic operation

Yaoting Xue[1,†], Jiasheng Cao[1,2,†], Tao Feng[1,†], Kaihang Zhang[1,†], Siyang Li[1], Jiahao Hu[2,3], Haotian Guo[1,4], Jinming Zhang[2,5], Yaoxian Song[1], Zhuofan Wang[1], Lei Wang[1], Qishan Huang[1], Haofei Zhou[1], Fanghao Zhou[1,6,7], Jiliang Shen[2], Yaowei Fan[1], Zhe Wang[1], Xinge Li[1,6], Jie-Wei Wong[1], Zhiwei Chen[8], Dongrui Ruan[1], Zhikun Miao[1], Bin Zhang[2], Enjie Zhou[2], Letian Gan[1], Xuanqi Wang[1], Ertai Cao[1], Tong Chen[1], Weifeng Zou[1], Junhui Zhang[8], Haojian Lu[9], Qinghai Zhang[7,10], Song Liu[11], Huixu Dong[4], Shiying Xiong[1], Shuyou Peng[2,12], Tuck-Whye Wong[1], Yuanjie Chen[13,14], Tiefeng Li[1,5,6,7,8,*], Mingyu Chen[2,3,*], Xuxu Yang[1,*], Wei Yang[1,*], Xiujun Cai[2,3,*]

1, Center for X-Mechanics, Department of Engineering Mechanics, Zhejiang University, Hangzhou, China

2, Department of General Surgery, Sir Run Run Shaw Hospital, Zhejiang University School of Medicine, Hangzhou, China

3, National Engineering Research Center of Innovation and Application of Minimally Invasive Instruments, Hangzhou, China

4, Grasp Lab, School of Mechanical Engineering, Zhejiang University, Hangzhou, China

5, First Affiliated Hospital of Zhejiang University, Zhejiang University School of Medicine, Hangzhou, China

6, State Key Laboratory of Ocean Sensing, Zhejiang University, Hangzhou, China

7, Institute of Fundamental and Transdisciplinary Research, Zhejiang University, Hangzhou, China

8, State Key Laboratory of Fluid Power and Mechatronic Systems, Zhejiang University, Hangzhou, China

9, Institute of Cyber-Systems and Control, Zhejiang University, Hangzhou, China

10, School of Mathematical Sciences, Zhejiang University, Hangzhou, China

11, School of Information Science and Technology, ShanghaiTech University, Shanghai, China

12, Department of General Surgery, the Second Affiliated Hospital, Zhejiang University, Hangzhou, China

13, Zhejiang Institute of Quality Science, Hangzhou, China

14, Zhejiang Provincial Key Laboratory of Digital Precision Measurement Technology, Hangzhou, China

[†] Yaoting Xue, Jiasheng Cao, Tao Feng, and Kaihang Zhang contributed equally to this work. All may be listed as first authors.

[*] Corresponding authors:

litiefeng@zju.edu.cn (Tiefeng Li)

mychen@zju.edu.cn (Mingyu Chen)

xxyang@zju.edu.cn (Xuxu Yang)

yangw@zju.edu.cn (Wei Yang)

srrsh_cxj@zju.edu.cn (Xiujun Cai)

Table of Contents

Note 1 Effects of plasticity in knotting

We found that plasticity primarily influences the preset stage, keeping the knot loop tight. In FEM simulation, both elastic and plastic effects are considered. Elasticity is simplified as linear elasticity, and plasticity is simplified as nonlinear isotropic/kinematic hardening model. To intuitively observe the effect of plasticity on the process of knot tightening and unloading, we simulate the model without plasticity. When the tying force F_{tying} is released, the knot loop relaxes and gradually expands, the knot is opened when the knot loop exceeds the slip loop (**Supplementary Fig. 23a**). With plasticity, the knot loop of the slipknot remains tightened after the release of F_{tying} (**Supplementary Fig. 23b**).

Note 2 Mechanical contact model of the slipknot

In this section, the two stages of the mechanical model are established and introduced in detail. In **Fig. 2f**, we present a schematic diagram of a 2D elastic rod subjected to external forces. The model divides the slipknot into a rod of total length $2L$ and a constraint with radius R, as represented by the black curve and the orange cylinder, respectively.

The Kirchhoff rod theory is commonly applied to predict the behavior of knots subjected to external forces[1,2]. In our model, the rod is assumed to be slender, satisfying condition $L \gg d$, enabling the reduction of 3D mechanics to a 1D representation of the rod's geometry and internal forces along its centerline arc length, $0 \leq s \leq L$. One notable difference between the model of strings and that of rods is, the rod possesses a bending stiffness of EI, with E being the Young's modulus and I the moment of inertia of the section. Note that, in our model, the filaments are treated as purely elastic. Although plasticity strongly influences slipknot tightening, its effect on the opening force warrants further investigation and is not addressed in the model. Although the rod can undergo a bending deformation, we assume that it is inextensible and unshearable, ensuring the centerline neither expands nor contracts, and its cross-sections stay orthogonal to the centerline during the bending deformation. Moreover, torsion and other out-of-plane deformations are ignored, simplifying the Kirchhoff rods to Euler elastica[3].

The rod is naturally straight at rest, and its extremities are loaded by the force F. The symmetry of the structure simplifies the analysis. A Frenet-Serret coordinate system is adopted along the rod, with s signifying the arc length and $\theta(s)$ denoting the turning angle. When an external force F is applied on the rod at $s = L$, the constraint stabilizes at position $s = l$. It is in contact with the rod, thereby generating pressure and friction forces. Since the structure of Stage 1 and Stage 2 are different, the constraint would not work in the same way. As described in the main text, it provides a tubular restraint for Stage 1, providing both contact force and contact moment and constraining the turning angle. However, for Stage 2, it forms a point constraint and provides only the contact force. The Coulomb friction coefficient between the rod and the constraint is labeled as μ, while F_c marks the general contact force prompted by the constraint. We now review the framework of Euler elastica, considering the kinematics, the force and the balance equations under concentrated loads.

The shape of the deformed elastic rod is represented by the position of its centerline. $\boldsymbol{r}(s) = x(s)\mathbf{e}_1 + y(s)\mathbf{e}_2$, where $\mathbf{e}_i$ denotes the basis vector along the i-direction. In the inextensible case that we consider, the kinematic relations between the position of the centerline and the turning angle, delineated by the transformation between the Frenet-Serret coordinate system and the Cartesian coordinate system, are

$$\frac{\mathrm{d}x(s)}{\mathrm{d}s} = \cos[\theta(s)], \frac{\mathrm{d}y(s)}{\mathrm{d}s} = \sin[\theta(s)], \tag{S1}$$

where the turning angle $\theta(s)$ is related to the curvature, $\boldsymbol{\kappa}(\mathrm{s}) = \theta'(s)\mathbf{e}_3$ of the rod's centerline. Note that the prime notation represents derivatives with respect to s. The internal loads along the rod centerline are reduced to an internal force, $\boldsymbol{N}$, and an internal moment, $\boldsymbol{M}$, applied to the cross-section at s. The moment-curvature constitutive relation of the rod is commonly described by

$$EI\boldsymbol{\kappa}(s) = \boldsymbol{M}(s), \tag{S2}$$

For Stage 2, since we have assumed the constraint to be point-contact, consequently it would exclude any distributed force. For Stage 1, since we begin from the far-end (nearly rest states) in our calculations, the length of the constraint is neglected because it is negligible in comparison with the total length of the rod. As a result, we assume for both Stage 1 and Stage 2, the contact of the rod with the constraint would not cause any distributed force. Under the equilibrium conditions of force and moment, the equations of Euler elastica are written as derived in

$$\boldsymbol{N}'(s) = 0, \tag{S3}$$

$$\boldsymbol{M}'(s) + \boldsymbol{r}'(s) \times \boldsymbol{N}(s) = 0, \tag{S4}$$

where

$$\boldsymbol{r}'(s) = \cos[\theta(s)]\mathbf{e_1} + \sin[\theta(s)]\mathbf{e_2}, \tag{S5}$$

denotes the derivative of position vector. For both Stage 1 and Stage 2, at position $s = l$, the constraint has a pressure force F_n and the Coulomb friction F_τ. Since the external force F is applied along the x-direction, the resultant of forces of the constraint, i.e., the direction of F_c, must also be along the x-direction considering the equilibrium of the rod. Then one obtains the expressions of $\boldsymbol{N}$

$$\boldsymbol{N}(s) = \begin{cases} (F - F_\text{c})\mathbf{e}_1 & 0 \le s \le l \\ F\mathbf{e}_1 & l < s \le L \end{cases}, \tag{S6}$$

Substituting Eqs. (S5), (S6) into Eq. (S4), we could get a piecewise second-order ordinary differential equation system for $\theta(s)$. To avoid any possible ambiguity, we define $\theta_1(s)$ on range $s \in [0, l]$ and $\theta_2(s)$ on range $s \in (l, L]$.

Accordingly,

$$\begin{cases} EI\theta_1''(s) - (F - F_c)\sin[\theta_1(s)] = 0 & 0 \le s \le l \\ EI\theta_2''(s) - F\sin[\theta_2(s)] = 0 & l < s \le L \end{cases}. \tag{S7}$$

In order to calculate each critical force F for each l, 6 boundary conditions for each stage in total are needed. First, for Stage 1, from the symmetry of such system, we have

$$\theta_1(0) = \pi, \tag{S8}$$

while for Stage 2 we have

$$\theta_1(0) = 0. \tag{S9}$$

For both Stage 1 and Stage 2, we have the following condition

$$\theta_1(l) = \theta_2(l), \tag{S10}$$

representing the continuity of the turning angle at the position $s = l$.

Next, the Coulomb's law of friction is applied. When the rod is about to have a relative slide with the constraint, we have $f = \mu F_n$, where f denotes the friction and F_n denotes the normal force. Since the resultant force is along the x-direction, we have the geometrical relation of the following.

$$F_n = F_c\sin[\theta(l)], F_\tau = F_c\cos[\theta(l)] = \mu F_n + f_i, \tag{S11}$$

with $i = 1$ for Stage 1 and $i = 2$ for Stage 2. f_i denotes the pre-friction caused by the pre-stress from the constraint, which is vital for the plateau period described in the main text and could be determined by experimental tests. Note that since the structure of

Stage 1 and Stage 2 are different, the values of f_1 and f_2 will not be identical. Details related to this subject will be given later. From Eq. (S11) we have

$$F_c = \frac{f_i}{\cos[\theta_1(l)] - \mu\sin[\theta_1(l)]}. \tag{S12}$$

Since we have taken the derivative of s while writing the governing equation Eq. (S7), the boundary conditions for bending moments are also needed. Considering that the diameter of the rod is relatively small, the friction is applied on the centerline and its additional contributions to the moment at $s = l$ are neglected. For Stage 1, we have

$$M_c = EI\theta_1'(l) - EI\theta_2'(l), \tag{S13}$$

while for Stage 2, we have

$$\theta_1'(l) = \theta_2'(l). \tag{S14}$$

For both Stage 1 and Stage 2, at $s = L$, we have

$$EI\theta_2'(L) = 0 \tag{S15}$$

The function of the constraint moment M_c constrains the turning angle at $s = l$, thus we have

$$\theta_1(l) = \theta_0 = \tan^{-1}\left(\frac{h_c}{2R}\right), \tag{S16}$$

which is determined through the geometry of the constraint, where h_c denotes the height of the constraint cylinder and $2R$ denotes its length.

Finally, the rigid constraint gives a position constraint along the x-axis, i.e.,

$$x(l) - x(0) = \int_0^l \cos[\theta_1(s)]\mathrm{d}s = 0, \tag{S17}$$

for Stage 1 and

$$x(l) - x(0) = \int_0^l \cos[\theta_1(s)]\mathrm{d}s = R, \tag{S18}$$

for Stage 2. Then Eq. (S7) together with Eqs. (S8), (S10), (S12), (S13), (S15), (S16) and (S17) gives the complete set of the equation system for Stage 1, while Eq. (S7) together with Eqs. (S9), (S10), (S12), (S14), (S15) and (S18) for Stage 2. For any given $l \in (0, L)$, solve the corresponding F and $x(L)$, thus getting the force-displacement curve.

In theoretical results, both Stage 1 and Stage 2 have asymptotic lines, i.e., when $l \to L$, also indicating $x \to -\infty$ (when L is sufficiently large), $\lim(F) = F_j$. Such phenomenon has also been verified by experimental results, as presented in **Fig. 2d**. To generate some comparability between the results of Stage 1 and Stage 2, we postulate these two stages have the same asymptotic line. Moreover, since they have different geometrical configurations, the situations at far-end, i.e., $x \to -\infty$ are modeled and presented in **Supplementary Fig. 24a, b**, respectively. We assume that the curves under the constraints are stress free, i.e., $\boldsymbol{N} = 0$, but the moments are not constrained, then the force conditions are labeled on this figure. For Stage 1, according to Eq. (S16), the turning angle at $s = l$ is fixed. Through Eq. (S12), we have

$$f_1 = F_j[\cos(\theta_0) - \mu\sin(\theta_0)]. \tag{S19}$$

However, for Stage 2, since the turning angle is not fixed, we have

$$f_2 = F_j = \frac{f_1}{[\cos(\theta_0) - \mu\sin(\theta_0)]}. \tag{S20}$$

The results of these two stages are both presented in **Fig. 2d**, their good agreement with experimental results indicates their applicability and reliability.

Although such model is in good agreement with the experiment, the governing equation Eq. (S7) exhibits strong nonlinearity and the integral constraint Eq. (S17) and (S18) complicates the calculations. A further simplified model is then established to capture the underlying mechanisms and provide valuable estimates. Assuming $F_c = F$, and ignore the deformation of rod at $l < s \leq L$. According to Eq. (S7), we will have $EI\theta_1''(s) = 0$, leading to $\boldsymbol{\kappa} = \theta_1'(\mathrm{s})\mathbf{e}_3 = \text{const}$. Such result indicates that the configuration of the rod will become the part of a circle, as presented in **Supplementary Fig. 24c**. The variational method is applied to find the relations between the applied external force F and the deformation. Taking the contact conditions χ and friction into consideration, we have

$$\delta U_{\mathrm{elas}} = \langle F - F_{\tau}, \delta x \rangle \tag{S21}$$

where symbol $\langle A, B \rangle$ denotes the inner product between A and B, and U_{elas} represents the elastic energy. We have

$$\delta U_{\mathrm{elas}} = \delta\left(\frac{1}{2}\int_{\Omega} \boldsymbol{\sigma} : \boldsymbol{\varepsilon} \mathrm{d}\Omega\right) = \langle F_{\mathrm{e}}, \delta x \rangle, \tag{S22}$$

where F_e denotes the equivalent elastic force. Moreover, since we have assumed that it is the bending energy that takes the lead, U_{elas} takes a further simplified form as

$$U_{\mathrm{elas}} = \int_0^l \frac{EI}{2}\frac{1}{R_t^{\,2}} \mathrm{d}s\,. \tag{S23}$$

Besides, the variational relation between x and l is

$$\delta x = -\delta l. \tag{S24}$$

The geometrical relation between the radius R_t and l is

$$l = R_{\mathrm{t}}(\pi - \theta) = R_{\mathrm{t}}\left(\pi - \arcsin\frac{R}{R_{\mathrm{t}}}\right) = p(R_{\mathrm{t}}), \tag{S25}$$

and the variational relation

$$\delta l = p'(R_{\mathrm{t}})\delta R_{\mathrm{t}}. \tag{S26}$$

Moreover, taking a closer look at the contact condition at $s = l$, since it will become singular for the turning angle θ, assume at the contact point, the turning angle will be $\theta = \varphi$. Applying Eq. (S11), and eliminating φ we will have

$$\left(\frac{F_{\tau} - f_2}{\mu F}\right)^2 + \left(\frac{F_{\tau}}{F}\right)^2 = 1, \tag{S27}$$

thus, we can express F_{τ} through F. Applying Eqs. (S22)-(S27) into Eq. (S21), finally we will get

$$F = F(g) = f_2 + g + \mu^2 g + \mu\sqrt{2f_2 g + g^2 + g^2\mu^2}, \tag{S28}$$

where

$$g = g(\theta) = \frac{EI}{2R^2}\frac{\big(\pi - \theta - \tan(\theta)\big)\sin^2(\theta)}{\pi - \theta + \tan(\theta)} = \frac{EI}{R^2}\cdot q(\theta), \tag{S29}$$

with the geometrical condition $R/R_{\mathrm{t}} = \sin(\theta)$ applied.

Inferring from the monotonicity analysis of Eq. (S28), F reaches its maximum when g reaches its apex. Since g depends on variable θ only, it reaches its apex when $q(\theta)$ becomes maximum. The image of $q(\theta)$ is presented in **Supplementary Fig. 25a**. We find it has no relation with any other parameters. As a result, we have

$$g_{\max} = c\frac{EI}{R^2}, \tag{S30}$$

where $c = 0.102092$ is a geometrical constant, denoting the maximum of $q(\theta)$. It tells that when $g(\theta)$ reaches its maximum, F also reaches its peak, which is actually the F_{peak} described in the main text.

A parametric study is conducted to assess the applicability of the simplified model. The comparison of Eq. (S28) with the outcomes of Stage 2, namely the original model, while keeping $EI = 1$, $R = 1$, and $f_2 = 0.1$ constant but altering the parameter μ, is depicted in **Supplementary Fig. 25b**. This comparison reveals that Eq. (S28) aligns closely with the results from Stage 2 for lower values of μ, with the curves intersecting at $\mu = 0.075$. Furthermore, with $EI = 1$, $R = 1$, and μ set to 0.075, the impact of varying f_2 is examined in **Supplementary Fig. 25c**, showing that the discrepancy is minimal. Continuing the analysis, with $\mu = 0.075$ and f_2 set to 0.1, changes in EI and R are explored in **Supplementary Fig. 25d**. The overlapping of the two surfaces demonstrates the effective representation of these parameters by Eq. (S28). The scales for force and length are 1 N and 1 mm, respectively.

In summary, while there are some discrepancies between Eq. (S28) and Stage 2, these differences are primarily related to frictional parameters. The parameters that govern bending correspond well. This suggests that the significant challenge in integrating knot theory into engineering practice stems from neglecting realistic contact conditions and frictional effects, whereas the bending aspects can be accurately modeled. Our work combines physical factors of elasticity F_e, contact χ, and friction f, together with the topology transformation $\mathcal{T}$ during the opening process of the slipknot, with a summarizing equation

$$F_{\text{peak}} = \mathcal{T} \circ \chi(F_e, f), \tag{S31}$$

to reveal our main considerations for the peak force F_{peak}

Note 3 Opening sliputures under dry, moist, and lubricated conditions

Surgical environments introduce variables such as moisture and lubrication that could alter the slipknot's performance regarding frictional behavior and tensile force limits. To understand this, we further studied the influence of friction in several filaments when they are in different working environments. Specifically, experiments characterizing the static friction of three filaments (PTFE monofilament, braided absorbable sutures (Vicryl), and braided non-absorbable sutures (Mersilk)) in four media (synthetic blood, simulated body fluid, natural saline, and silicone oil) were conducted. The frictional coefficient parameter μ was tested through the apparatus described in **Extended Data Fig. 3**, and the parameter f_2 is derived from the corresponding tensile tests of the slipknot (**Supplementary Table 2-4**).

We measured the friction coefficient of the lines in various volumes of liquids (**Extended Data Fig. 3b-e**). The friction coefficients of PTFE fluorocarbon monofilament and Vicryl exhibited little change (< 10%) in synthetic blood, simulated body fluid, and natural saline as compared to the dry condition. However, in silicone oil, the friction coefficients of PTFE decreased by 27.737%, and that of Vicryl increased by 14.805%, respectively. The friction coefficient of Mersilk was approximately 100% higher in synthetic blood, simulated body fluid, and natural saline than that in the dry condition, while it decreased by 17.853% in silicone oil.

We next tested F_{peak} of the slipknots when they were submerged in different liquids, and fabricated with various values of F_{tying}. For PTFE, F_{peak} exhibited no measurable change in the three aqueous media (synthetic blood, simulated body fluid, natural saline), while a remarkable reduction in silicone oil; for Mersilk, F_{peak} exhibited a slight increase in three aqueous media and some reduction in silicone oil; and for Vicryl, F_{peak} increased in all four liquids, with the largest increment in silicone oil. We found that the theoretical model is applicable for predicting the peak force of slipknots fabricated from both monofilament filaments and braided sutures, and the results largely mirror the friction trends predicted by the analytical model (**Supplementary Table 5-8**), particularly in silicone oil, where the model accurately predicted the increase and decrease for all three filaments. However, for Mersilk in aqueous media, the theoretical outcome leads to a higher prediction compared to the actually measured increase. Such discrepancy is potentially due to the model not accounting for the effect of swelling on the radius of constraint, R, in Eq. (S30), which could overestimate the peak force.

Note 4 Suture-tissue contact model

The appearance of the repaired tissue and its blood supply are attributed to the pressure distribution. A monotonic increase in contact pressure in conventional continuous sutures was observed (**Extended Data Fig. 7a**). Here we develop a model to analyze the distribution of the contact pressure between the suture and the tissue, as shown in **Extended Data Fig. 7b**. Let R represent the radius of the tissue, p_0 the preload caused by the tissue deformation per unit thickness of the suture, θ the angle swept by turns of the suture measured in radians. Governing equations for the tension in the suture, T, and the internal pressure between the suture and the tissue p, are listed as follows:

$$p(\theta)R = T(\theta) + p_0 R, T'(\theta) = \mu p(\theta) R, T(0) = T_0, \tag{S32}$$

and the solutions are

$$p(\theta) = e^{\mu\theta}\left(p_0 + \frac{T_0}{R}\right), T(\theta) = e^{\mu\theta} T_0 + e^{\mu\theta} p_0 R - p_0 R, \tag{S33}$$

from which an exponential relationship among p, T, and θ can be observed. This model predicts that the contact pressure p increases as θ increases, a trend that has been verified with the extracted pressure data (**Extended Data Fig. 7c**).

This model also provides a quantitative link between the two sides of the sliputure. The side with the slipknot was pulled and is defined as the active side, whereas the other side without the slipknot was held stationary and is referred to as the fixed side. From Eq. (S33) we have

$$\frac{p_{\text{fixed}}}{p_{\text{active}}} = e^{-\mu\pi} \approx \frac{T_{\text{fixed}}}{T_{\text{active}}} < 1, \tag{S34}$$

which predicts that the force on the fixed side will be consistently lower than that on the active side. For the tested friction coefficient between the suture and the silicone practice model, μ = 0.283 ± 0.003, we obtain $T_{\mathrm{fixed}}/T_{\mathrm{active}}$ = 0.411, which aligns well with experimental observations ($T_{\mathrm{fixed}}/T_{\mathrm{active}}$ = 0.420 ± 0.176) (**Supplementary Fig. 22**).

Note 5 Feasible force range prediction

The feasible force range lies between two important values: the lower limit to prevent from dehiscence, and the upper limit to prevent from ischemia (**Fig. 3c**). These two values are determined through experiments in the main text. Here, we present two mechanical models that can explain the underlying mechanism.

The lower tension limit is to prevent dehiscence. We apply the thin-walled column model for prediction (**Supplementary Fig. 26a**). Assume the diameter of the column is D, the thickness is δ, and it is filled with gas with inner pressure p, given that N stitches are applied in a suture area of A. The stress tensor can be expressed by:

$$\sigma = \begin{bmatrix} \sigma_1 & 0 \\ 0 & \sigma_2 \end{bmatrix}, \tag{S35}$$

where we have:

$$\sigma_1 = \frac{pD}{4\delta}, \sigma_2 = \frac{pD}{2\delta}, \tag{S36}$$

and the traction can be expressed by:

$$t = \sigma \cdot n. \tag{S37}$$

the force required in the suture to maintain the inner pressure is obtained as:

$$F = (\sigma_1 \sin^2\theta + \sigma_2 \cos^2\theta) A/N. \tag{S38}$$

The upper limit to prevent from ischemia. Here we adopt the model to predict the critical force of tearing the tissue (**Supplementary Fig. 26b**). The radius of the suture is R, and a tying force per unit length F is applied on center of the suture. Young's modulus and Poisson's ratio of the suture are E_1 and ν_1, and those for the tissue are E_2 and ν_2, respectively.

From previous work[4,5], the contact pressure $p(\theta)$ can be expressed by

$$\frac{p(\theta)}{F/R} = \frac{2\sqrt{b^2 - y^2}}{\pi\sqrt{b^2+1}(1+y^2)} + \frac{1}{\pi}\left(1 - \frac{B}{2}\right)\ln\left(\frac{\sqrt{b^2+1} + \sqrt{b^2 - y^2}}{\sqrt{b^2+1} - \sqrt{b^2 - y^2}}\right), \tag{S39}$$

where $y = \tan(\theta/2)$, and

$$B = \frac{2b^4 + 2b^2 - 1}{b^2(b^2+1)} \tag{S40}$$

The parameter b can be obtained through

$$\frac{(\alpha - 1)(\ln(b^2+1) + 2b^4) + 2}{\pi(1+\alpha)(b^2+1)b^2} - \frac{4\beta}{\pi(1+\alpha)} = 0, \tag{S41}$$

where α and β are defined through

$$\alpha = \frac{((\kappa_1+1)/\mu_1) - ((\kappa_2+1)/\mu_2)}{((\kappa_1+1)/\mu_1) + ((\kappa_2+1)/\mu_2)}, \beta = \frac{((\kappa_1-1)/\mu_1) - ((\kappa_2-1)/\mu_2)}{((\kappa_1+1)/\mu_1) + ((\kappa_2+1)/\mu_2)}. \tag{S42}$$

For plane stress situations, we have

$$\kappa_i = \frac{3 - \nu_i}{1 + \nu_i}, \mu_i = \frac{E_i}{2(1+\nu_i)}, \tag{S43}$$

and for plane strain situations, we take

$$\kappa_i = 3 - 4\nu_i, \mu_i = \frac{E_i}{2(1+\nu_i)}, \tag{S44}$$

The stress field at the contact surface $(r = R)$ is then given by

$$\sigma_{rr}(\theta) = -p(\theta), \sigma_{r\theta}(\theta) = 0, \tag{S45}$$

and

$$\sigma_{\theta\theta}(\theta) = -p(\theta) + \frac{3 - \nu_2^*}{2\pi}\cos(\theta) + \frac{\ln(b^2+1) + 2b^4}{\pi b^2(b^2+1)}. \tag{S46}$$

Note that, we have $\nu_2^* = \nu_2$ for the plane stress situation, and we take $\nu_2^* = \nu_2/(1-\nu_2)$ for the plane strain case.

Converting the stress tensor into the x-y plane

$$\begin{cases} \sigma_{xx}(\theta) = \dfrac{\sigma_{rr} + \sigma_{\theta\theta}}{2} + \dfrac{\sigma_{rr} - \sigma_{\theta\theta}}{2}\cos(2\theta), \\ \sigma_{yy}(\theta) = \dfrac{\sigma_{rr} + \sigma_{\theta\theta}}{2} - \dfrac{\sigma_{rr} - \sigma_{\theta\theta}}{2}\cos(2\theta), \\ \sigma_{xy}(\theta) = \dfrac{\sigma_{rr} - \sigma_{\theta\theta}}{2}\sin(2\theta). \end{cases} \tag{S47}$$

The dimensionless von Mises stress can then be expressed by

$$\sigma_M(\theta) = \sqrt{\frac{1}{2}\begin{pmatrix} \left(\sigma_{xx}(\theta) - \sigma_{yy}(\theta)\right)^2 + \left(\sigma_{yy}(\theta) - \sigma_{zz}(\theta)\right)^2 \\ +\left(\sigma_{zz}(\theta) - \sigma_{xx}(\theta)\right)^2 + 6\left(\sigma_{xy}(\theta)\right)^2 \end{pmatrix}}, \tag{S48}$$

where for plane stress condition, we have $\sigma_{zz}(\theta) = 0$, and for plane strain condition, we take

$$\sigma_{zz}(\theta) = \nu_2\left(\sigma_{xx}(\theta) + \sigma_{yy}(\theta)\right). \tag{S49}$$

The lower tension limit is obtained when the maximum of $\sigma_M(\theta)$ reaches the strength of a tissue $[\sigma]$, which can be represented by:

$$\max[\sigma_M(\theta)] = [\sigma]. \tag{S50}$$

Supplementary References

1 Moulton, D. E., Grandgeorge, P. & Neukirch, S. Stable elastic knots with no self-contact. *J Mech Phys Solids* **116**, 33-53 (2018).

2 Jawed, M. K., Dieleman, P., Audoly, B. & Reis, P. M. Untangling the mechanics and topology in the frictional response of long overhand elastic knots. *Phys Rev Lett* **115**, 118302 (2015).

3 Grandgeorge, P., Sano, T. G. & Reis, P. M. An elastic rod in frictional contact with a rigid cylinder. *J Mech Phys Solids* **164**, 104885 (2022).

4 Ciavarella, M. & Decuzzi, P. The state of stress induced by the plane frictionless cylindrical contact. I. The case of elastic similarity. *Int. J. Solids Struct.* **38**, 4507–4523 (2001).

5 Ciavarella, M. & Decuzzi, P. The state of stress induced by the plane frictionless cylindrical contact. II. The general case (elastic dissimilarity). *Int. J. Solids Struct.* **38**, 4525–4533 (2001).

Supplementary Figures

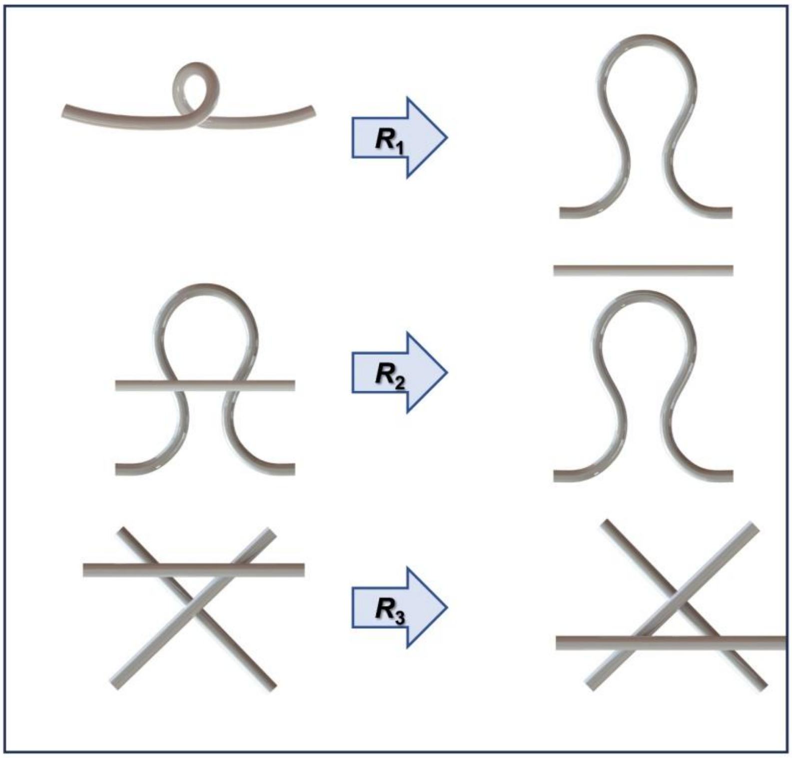

Supplementary Fig. 1: A schematic diagram of the three topology-preserving Reidemeister moves.

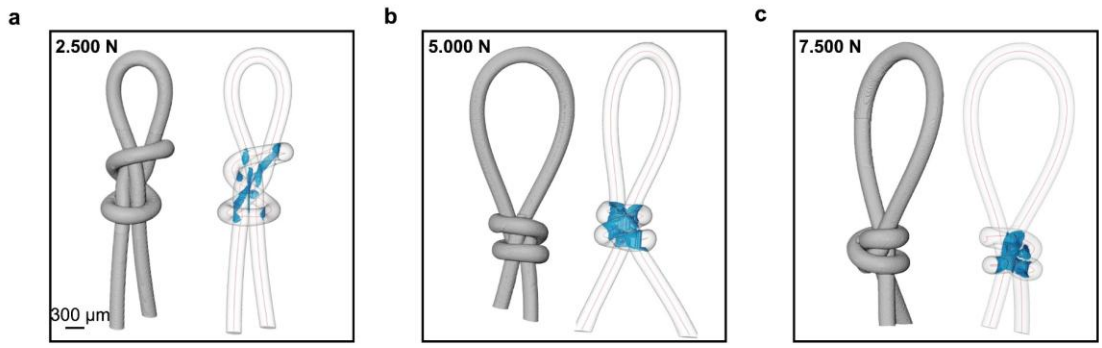

Supplementary Fig. 2: Micro-CT scans of the slipknots with different F_{tying} values. **a,** 2.500 N. **b,** 5.000 N. **c,** 7.500 N. The blue area represents the self-contact region within the slipknot, with contact areas of 1042034 μm^2 for 2.500 N **(a)**, 1703628 μm^2 for 5.000 N **(b)**, and 2411933 μm^2 for 7.500 N **(c)**.

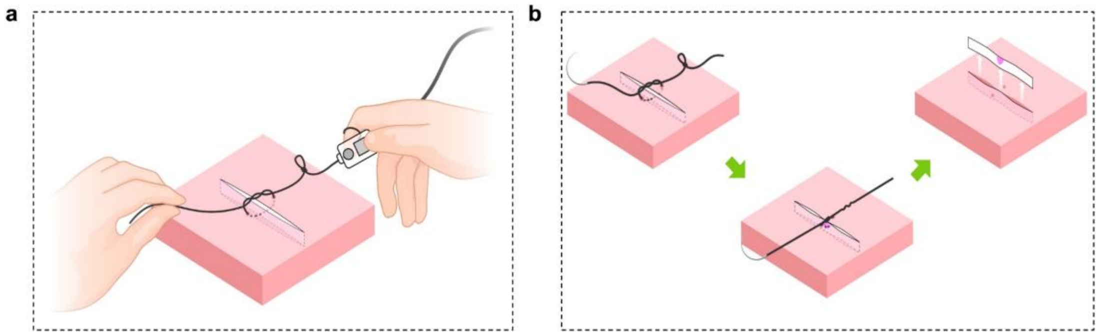

Supplementary Fig. 3: A schematic illustration of knot tying force test (a) and incision pressure test (b). a, Surgeons repair the simulated wound with force information collected by the real-time dynamometer. **b,** After repairing the simulated wound, the exerted pressure on both sides of the wound lead to a visible color demonstration in pressure-sensitive films, indicating the incision pressure.

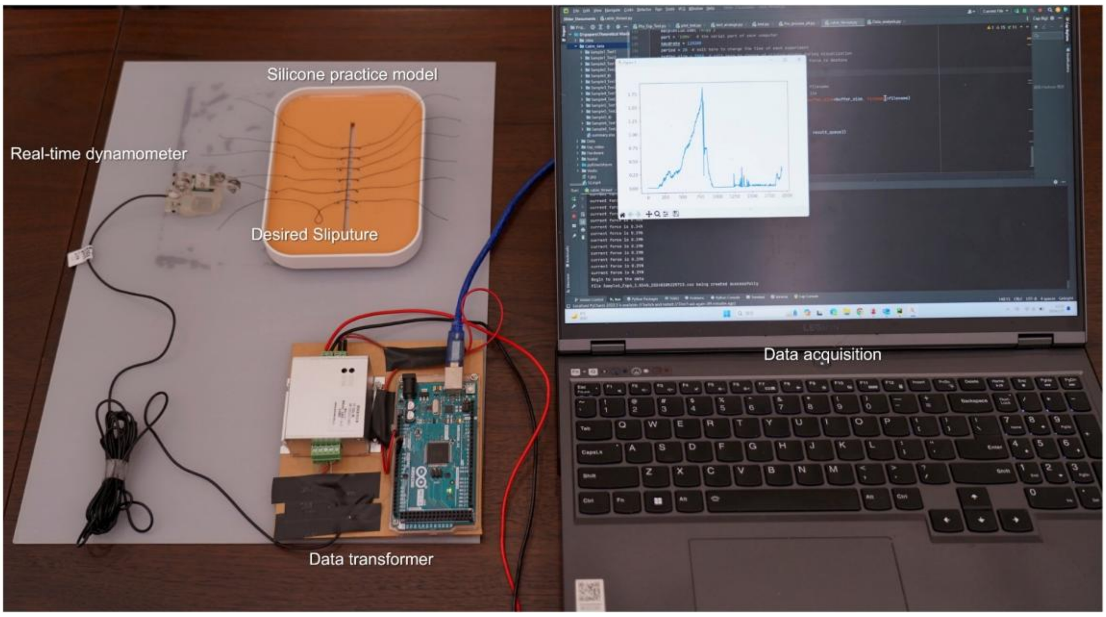

Supplementary Fig. 4: The knot tying force test platform for evaluating both the knotting force accuracy and incision pressure.

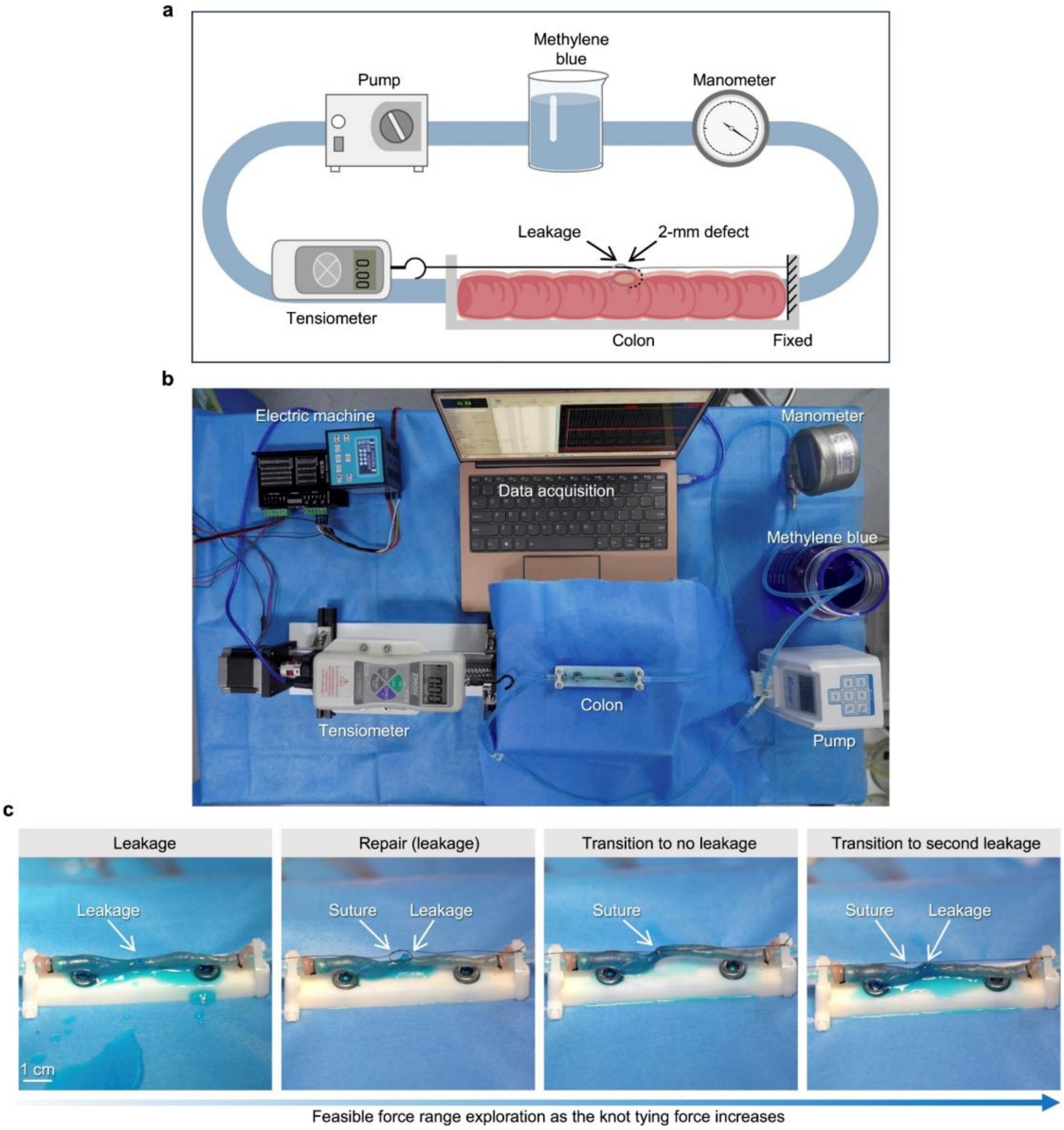

Supplementary Fig. 5: Exploration for feasible force range in *ex vivo* repair of colonic defects in a rat model. a, b, The mechanical test platform for feasible force range, including tissues to be tested, tensiometer, electric machine, pump, manometer, and phosphate buffered saline dissolving methylene blue. **c,** A schematic illustration of exploring the feasible force range of tissues. Feasible force range is determined by force at the transition to no leakage (F_{min}) and force at transition to second leakage (F_{max}) as the knot tying force increases.

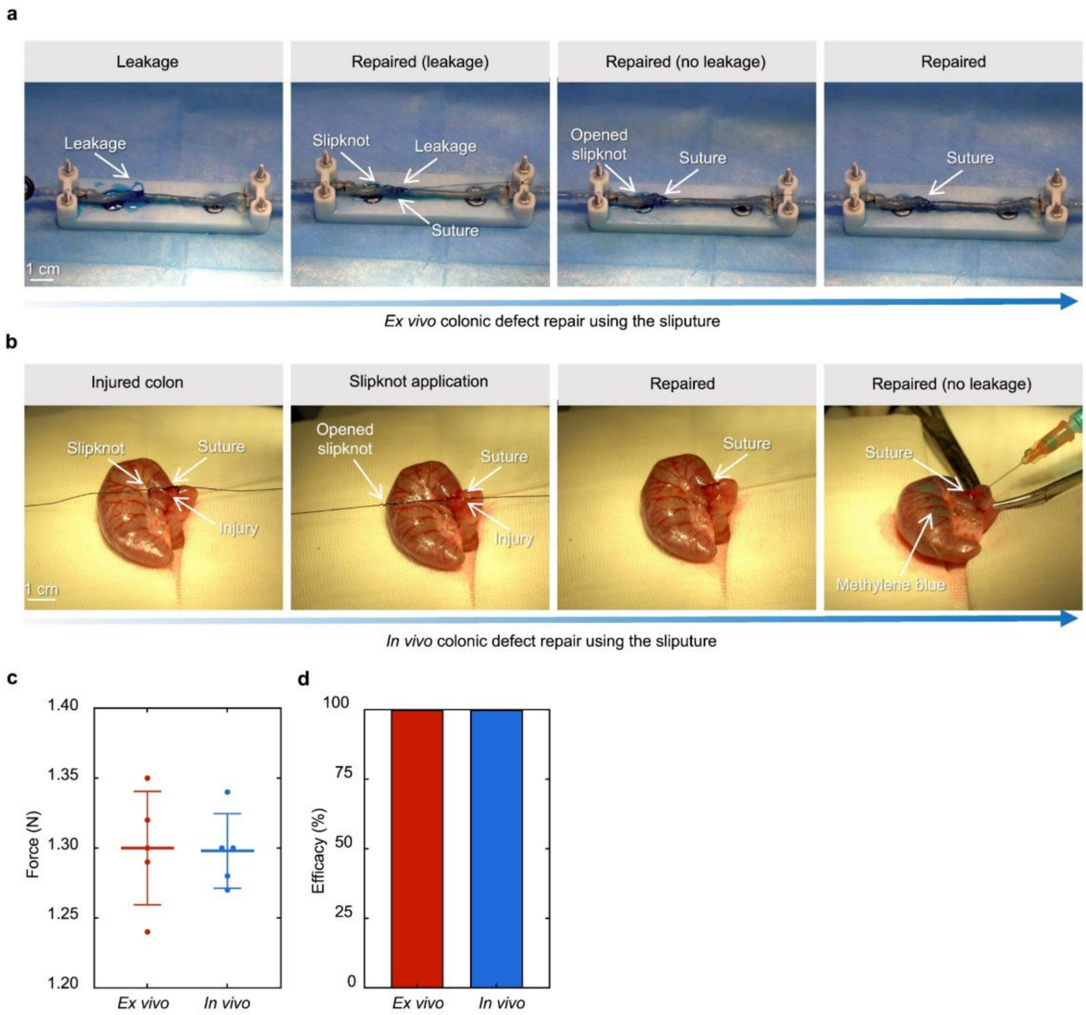

Supplementary Fig. 6: Mechanical comparison of *ex vivo* and *in vivo* colonic defects model repaired by sliputures. a, b, Schematic illustrations of *ex vivo* (**a**) and *in vivo* (**b**) colonic defects model repaired by sliputures based on the visual signal. **c, d,** The comparison of force output (1.30 ± 0.04 N *vs.* 1.30 ± 0.03 N, $P = 0.93$) (**c**) and efficacy (100% *vs.* 100%, $P > 0.99$) (**d**) between *ex vivo* and *in vivo* groups. Values in **c** represent the mean and the s.d. (n = 5; independent biological replicates). P values were determined by Student's t-test. Values in **d** are shown as percentages (n = 5; independent biological replicates).

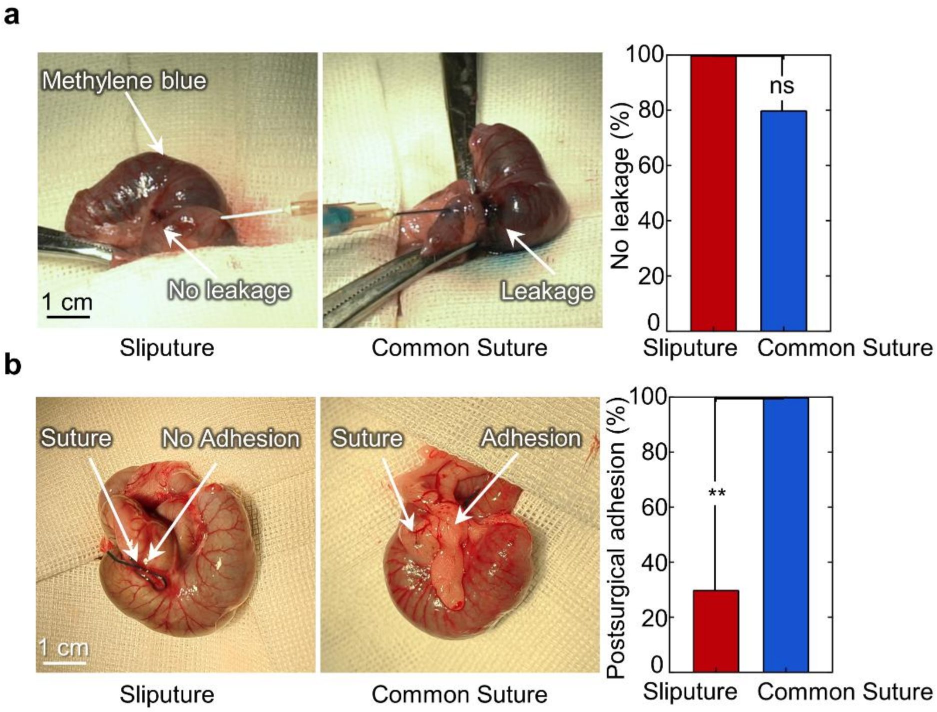

Supplementary Fig. 7: Comparison of the mechanical influence on surgery-related complications between sliputure and common suture. a, **b**, Comparison of the mechanical influence on leakage (**a**) and adhesion rates (**b**) after being repaired by sliputures and common sutures. ns, not significant; **, $P < 0.01$. Values in **a, b** are shown as percentages. (n = 10; independent biological replicates). P values were determined by Fisher's exact test.

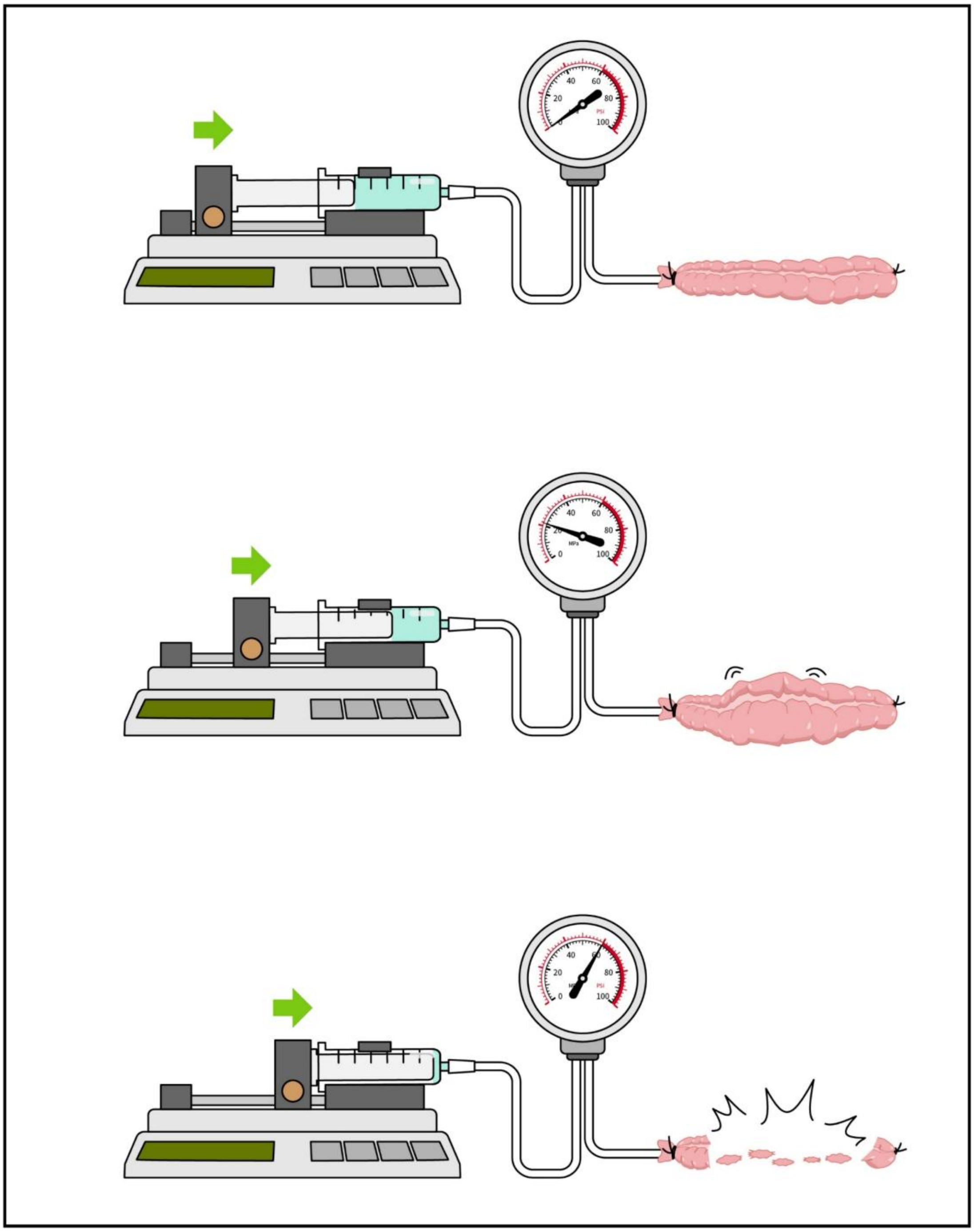

Supplementary Fig. 8: A schematic illustration of colonic burst pressure measurement. The tissue sample is placed in a burst pressure device and phosphate buffered saline dissolving methylene blue is infused at a constant rate of 10 mL/min until the pressure cause failure. During measurement, peak burst pressure is identified when fluid leak occurs.

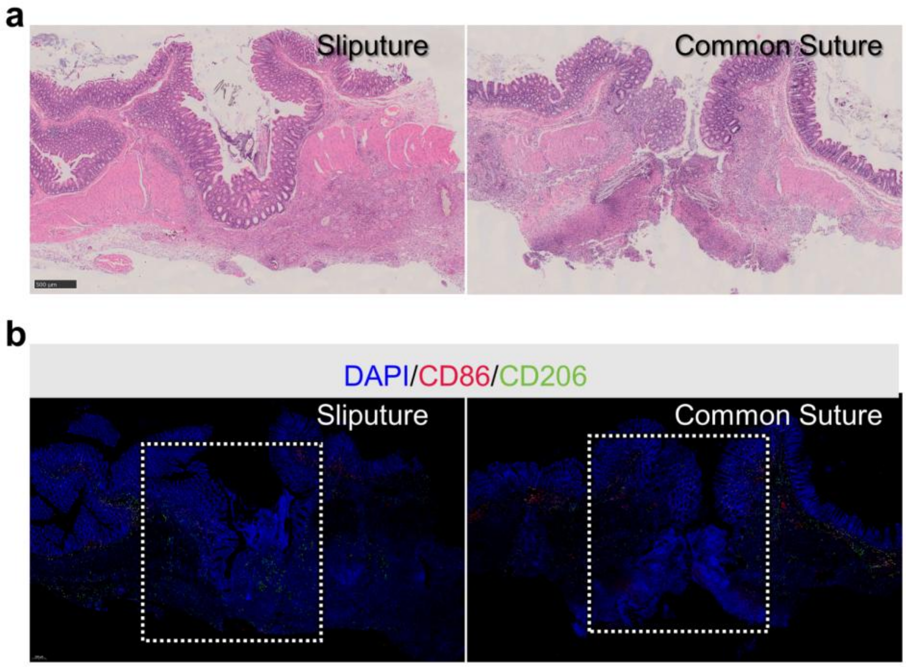

Supplementary Fig. 9: The impact of sliputure on wound healing in vivo. a, H&E staining for detecting tissue healing status of the rat colonic defect repaired by sliputures and common sutures. **b**, MIF staining for detecting pro-inflammatory macrophage (CD86) and anti-inflammatory macrophage (CD206) of the rat colonic defect repaired by sliputures and common sutures. Dashed lines indicate the repaired defects. Scale bars, 500 μm (**a**), 200 μm (**b**). MIF: Multiplex immunofluorescence.

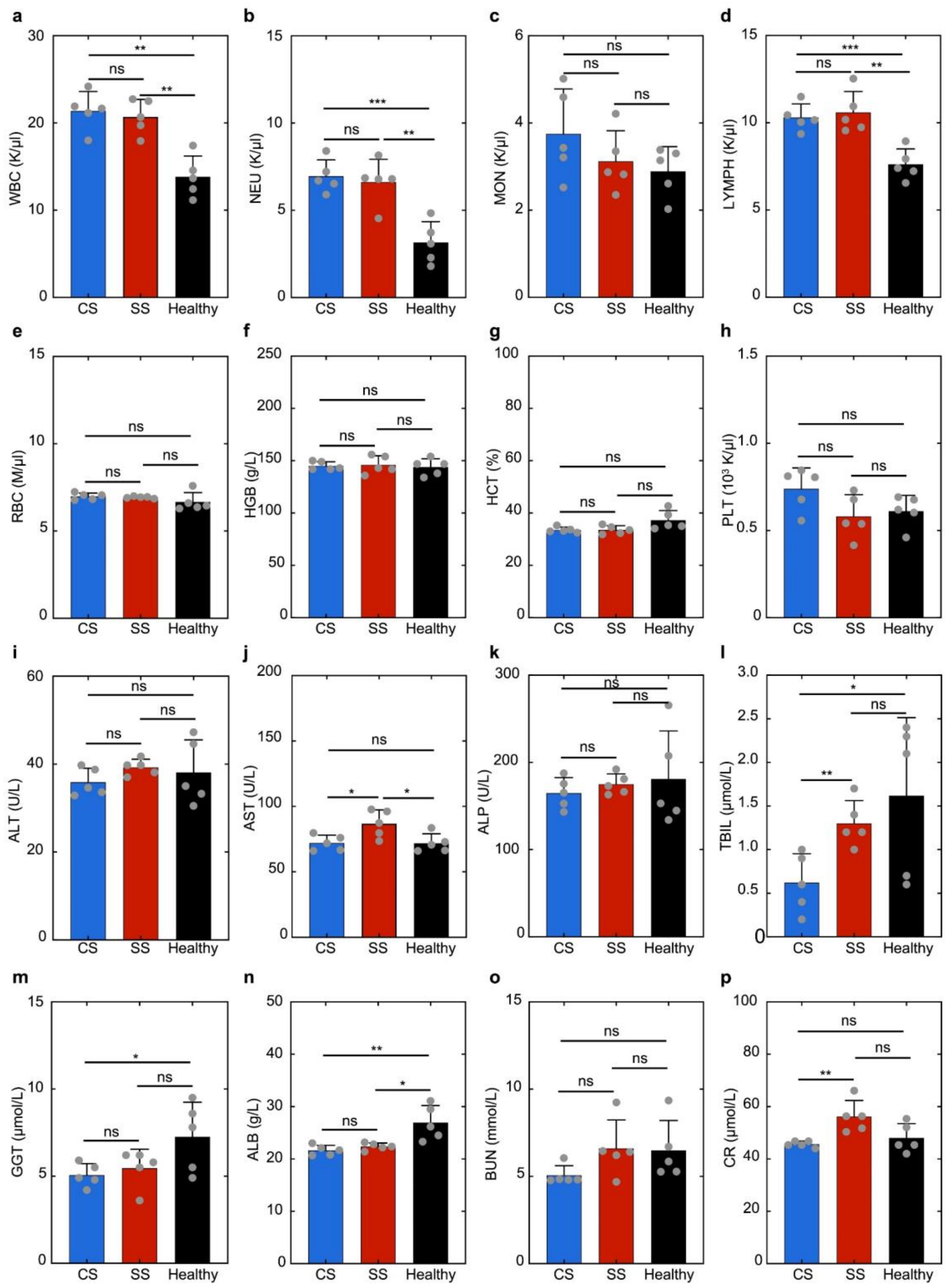

Supplementary Fig. 10: Blood analysis. a, White blood cell count. **b,** Neutrophil. **c,** Monocyte. **d,** Lymphocyte. **e,** Red blood cell count. **f,** Hemoglobin. **g,** Hematocrit. **h,** Platelet count. **i,** Alanine aminotransferase. **j,** Aspartate aminotransferase. **k,** Alkaline phosphatase. **l,** Total bilirubin. **m,** γ-glutamyl transpeptidase. **n,** Albumin. **o,** Blood urea nitrogen. **p,** Creatinine. SS, Sliputure; CS, Common suture. ns, not significant; *, $P < 0.05$; **, $P \leqslant 0.01$; ***, $P \leqslant 0.001$. Values in **a, b** represent the mean and the s.d. (n = 10; independent biological replicates). P values were determined by Student's t-test.

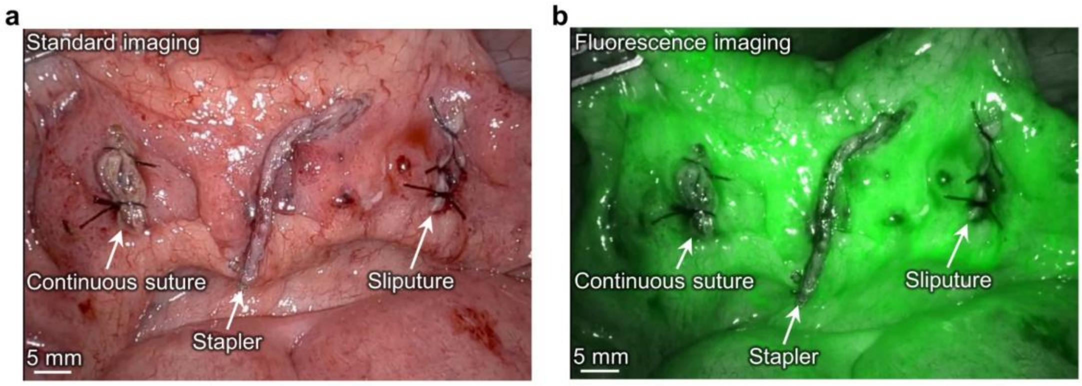

Supplementary Fig. 11: The images of live porcine colonic repair by continuous suture, stapler, and sliputure under a robotic system. a, Tissue appearance under standard imaging. **b,** Tissue appearance under fluorescence imaging 60 s post-injection of indocyanine green. Scale bars, 5 mm.

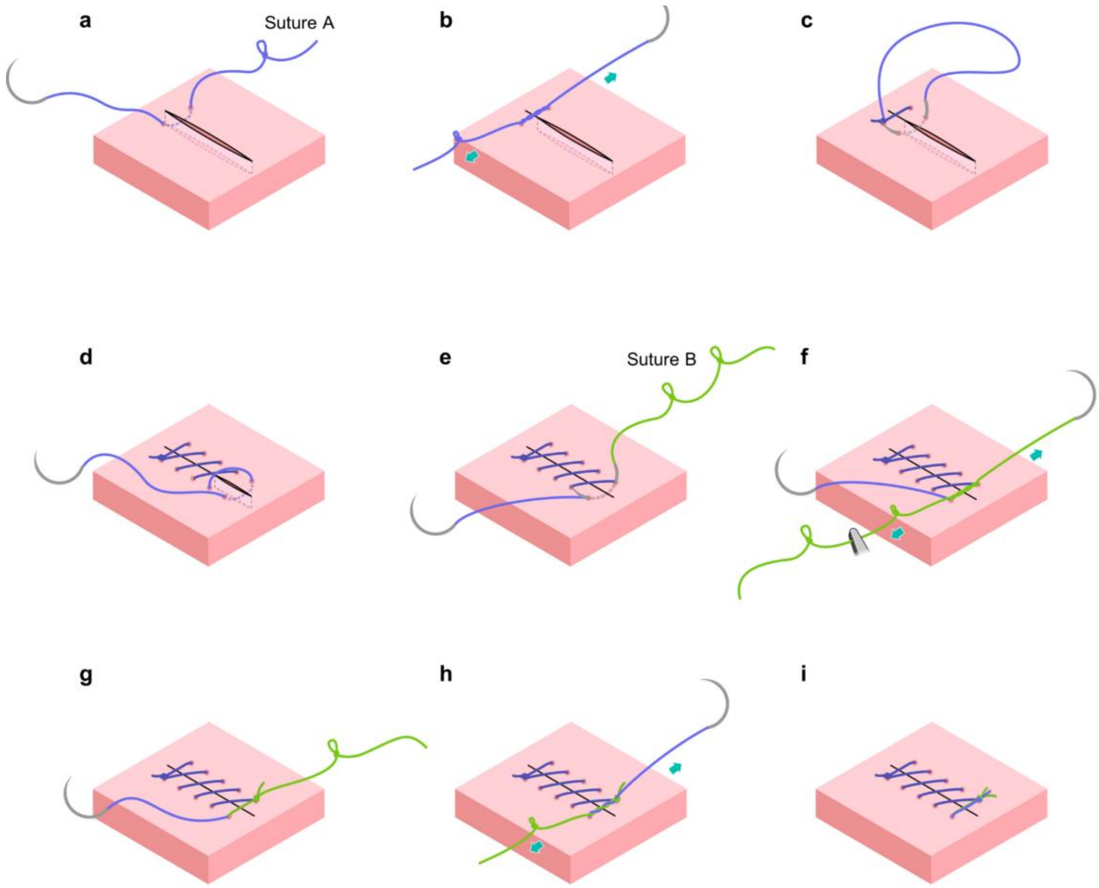

Supplementary Fig. 12: Sliputures for continuous sutures protocol. a, Use a sliputure (Suture A) to place the first stitch. **b**, Tie an anchor knot at the proximal end of the incision until the slipknot is opened. **c, d**, Perform continuous sutures of 4 stitches as usual, leaving the final stitch unknotted. **e**, Use another sliputure with two slipknots (Suture B) to place one stitch at the distal end of the incision. **f**, Use the slipknot near the incision to form an anchor knot. **g, h**, Tie Suture A and Suture B (remains one slipknot) together to complete the final knot. **i**, Finished continuous sutures with sliputures.

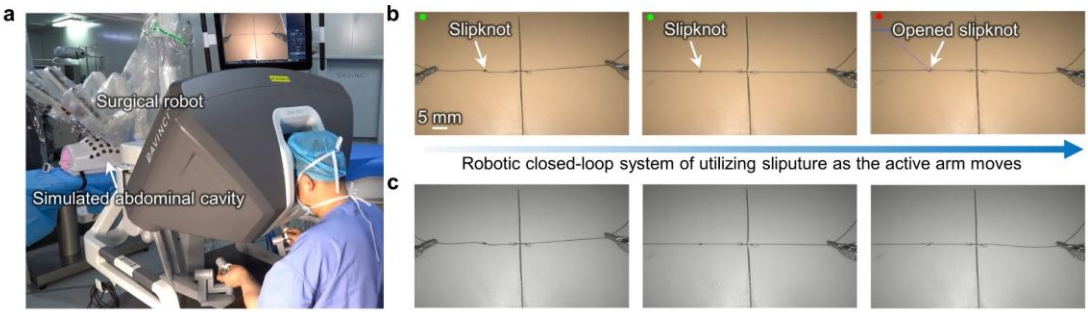

Supplementary Fig. 13: Validation of the vision-based automatic-braking experiment in the silicone practice model. a, The surgeon employs sliputures to repair the silicone practice model using the da Vinci robotic system under real-time monitoring. **b**, **c**, The system-triggered red stop marker was activated upon slipknot opening as the active arm moved on the silicone practice model.

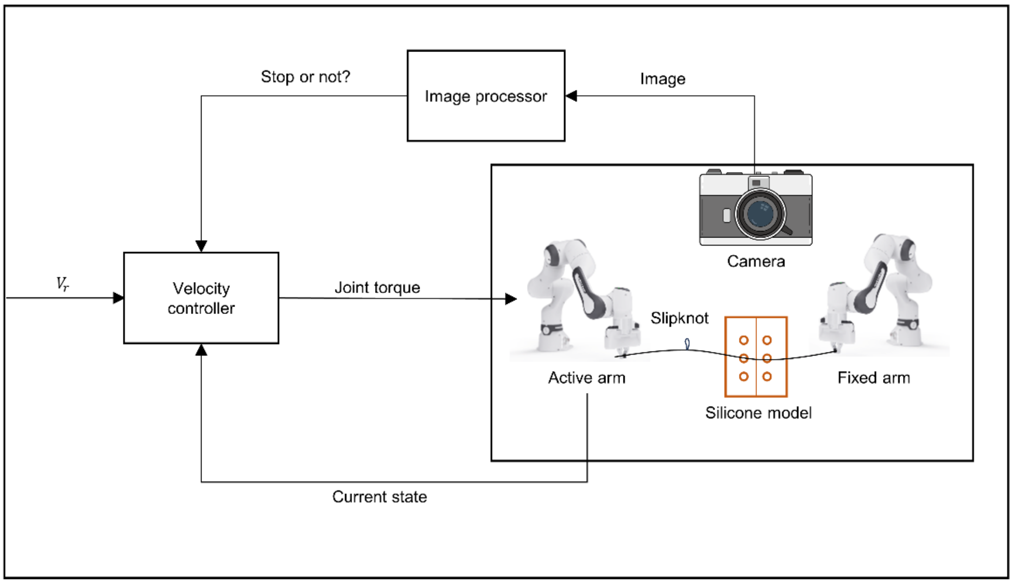

Supplementary Fig. 14: The overall framework of slipknot gauged intelligent operation without human intervention.

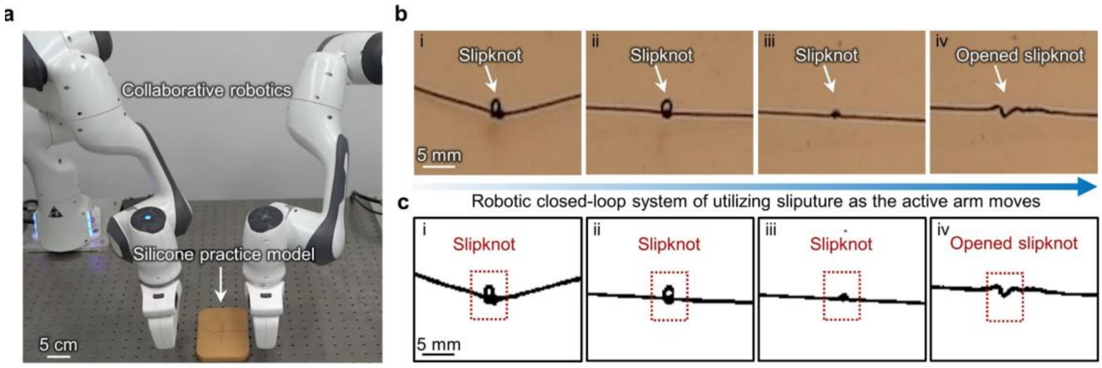

Supplementary Fig. 15: Sliputure-assisted intelligent operation without human intervention. a, b, Industrial robots with an image processing system operate a sliputure without human intervention, demonstrating vision-based intelligence. **c**, The images of the sliputure are captured by the intelligent system for processing.

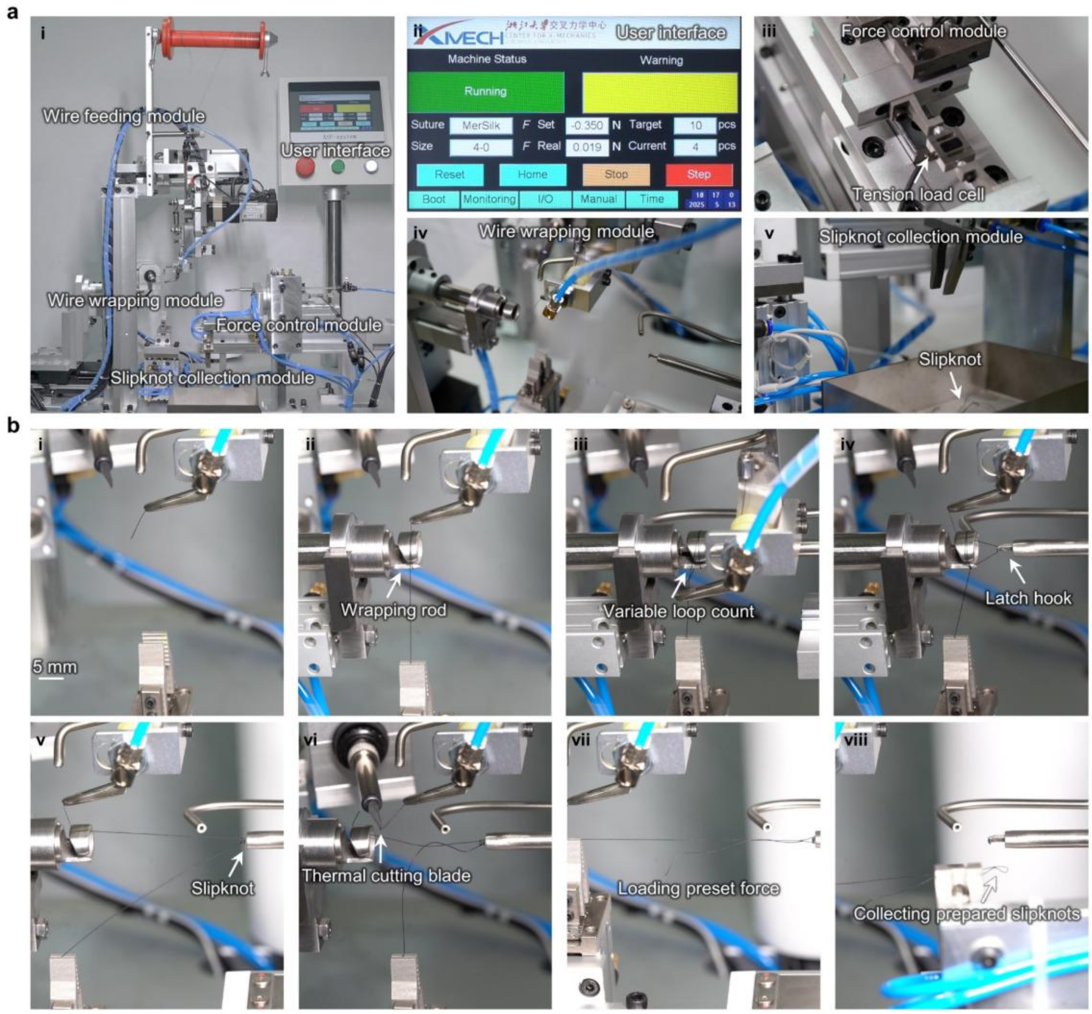

Supplementary Fig. 16: Automatic Slipknot Fabrication System (ASF-system). (a), **(i)** Overall view of the ASF-system, which integrates modules for wire feeding, force control, wire wrapping, slipknot collection, and a user interface. **(ii)** The user interface allows selection of suture material, diameter, F_{tying}, and slipknot quantity, with built-in algorithms optimizing control parameters. **(iii)** Force control module utilizing a tension load cell in conjunction with a servo motor to accurately apply the preset tension. **(iv)** The wire wrapping module employs a wrapping rod that coils suture material furnished by the wire feeding module; loop count is adjustable (single, double, or multiple loops). The final loop is placed into a dedicated groove, enabling the latch hook to capture and pull the suture tail, completing the slipknot structure. **(v)** Slipknot collection module uses a pneumatic gripper to hold the non-knot portion of the suture, carefully controlling grip force to avoid material damage, subsequently placing completed slipknots into a storage tray. **(b)** Operational sequence for automated batch slipknot production. **(i)** Wire feeding module grips the suture tail. **(ii)** Wrapping rod extends and the suture is coiled around it for a preset number of loops. **(iii)** The final half-loop is placed into a groove; the latch hook then enters and captures the suture tail. **(iv)** Latch hook withdraws, forming the slipknot geometry. **(v)** Latch hook locks the suture tail in position. **(vi)** A thermal cutting blade trims excess suture material, simultaneously sealing its end. **(vii)** The tension load cell, servo motor, and linear actuator apply the predefined F_{tying}. **(viii)** After securing the suture with the pneumatic gripper at a defined location, the latch hook releases, and a pneumatic device ejects the slipknot into storage. This automated cycle repeats continuously, facilitating high-throughput, standardized slipknot production from bulk suture materials.

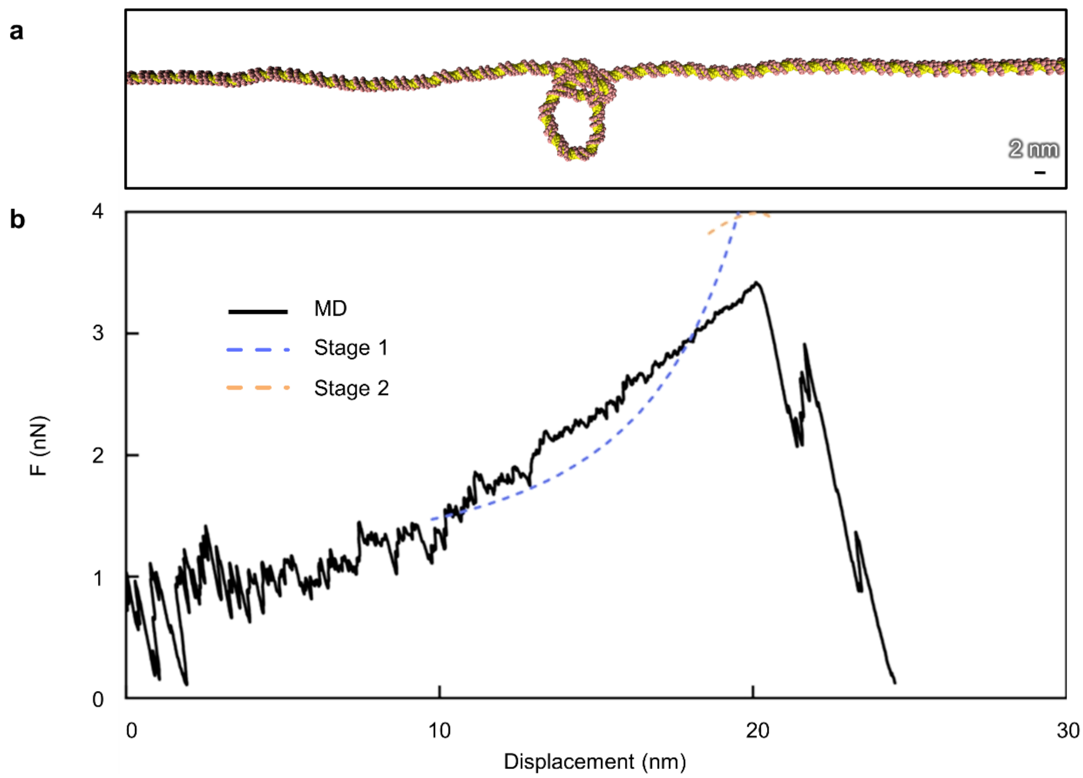

Supplementary Fig. 17: DNA slipknot molecular dynamics (MD) simulation and theoretical model. a, The DNA slipknot in MD simulation. **b,** The results of MD simulation and theoretical model.

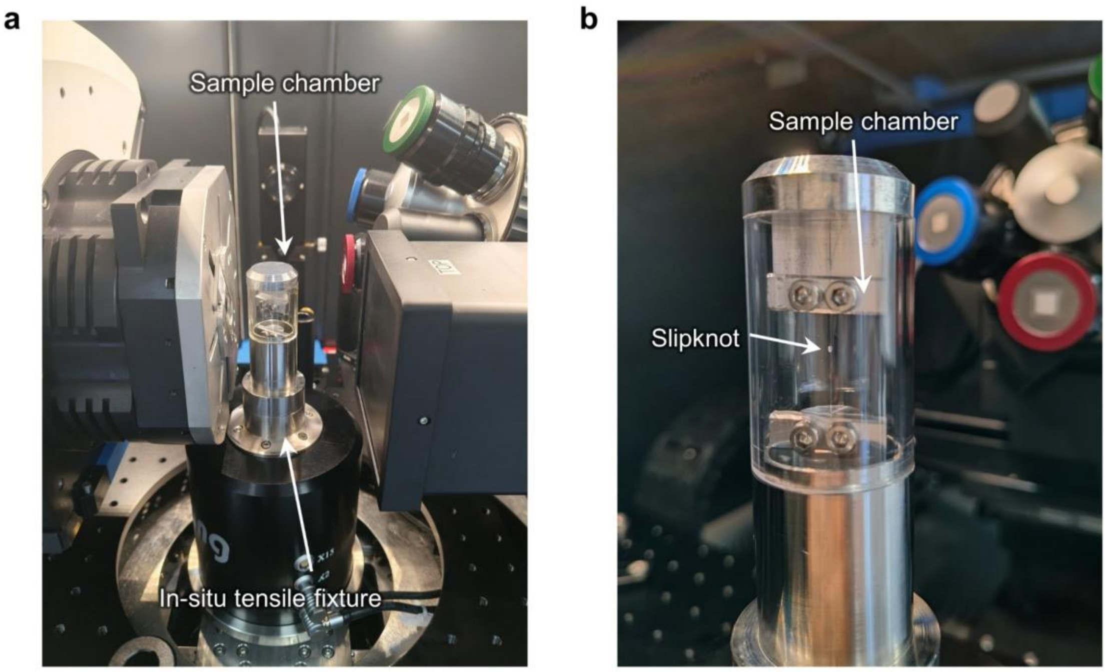

Supplementary Fig. 18: Fixture for in situ measurement of the slipknot opening process in micro-CT. a, An in situ tensile fixture that fits within the sample chamber of the micro-CT scanner. The fixture allows to preset tensile force to the slipknot. While gradually releasing, the configurations of the slipknot are scanned. **b**, The slipknot inside the sample chamber.

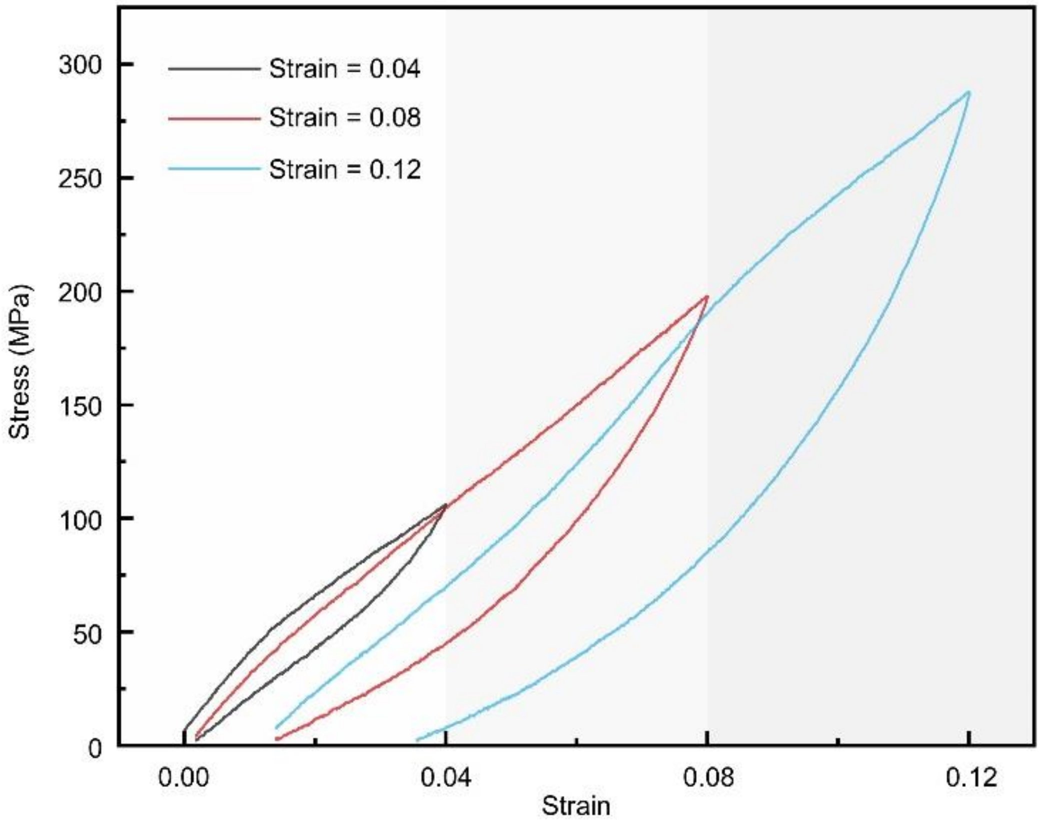

Supplementary Fig. 19: Cyclic tensile test data of fluorocarbon monofilament.

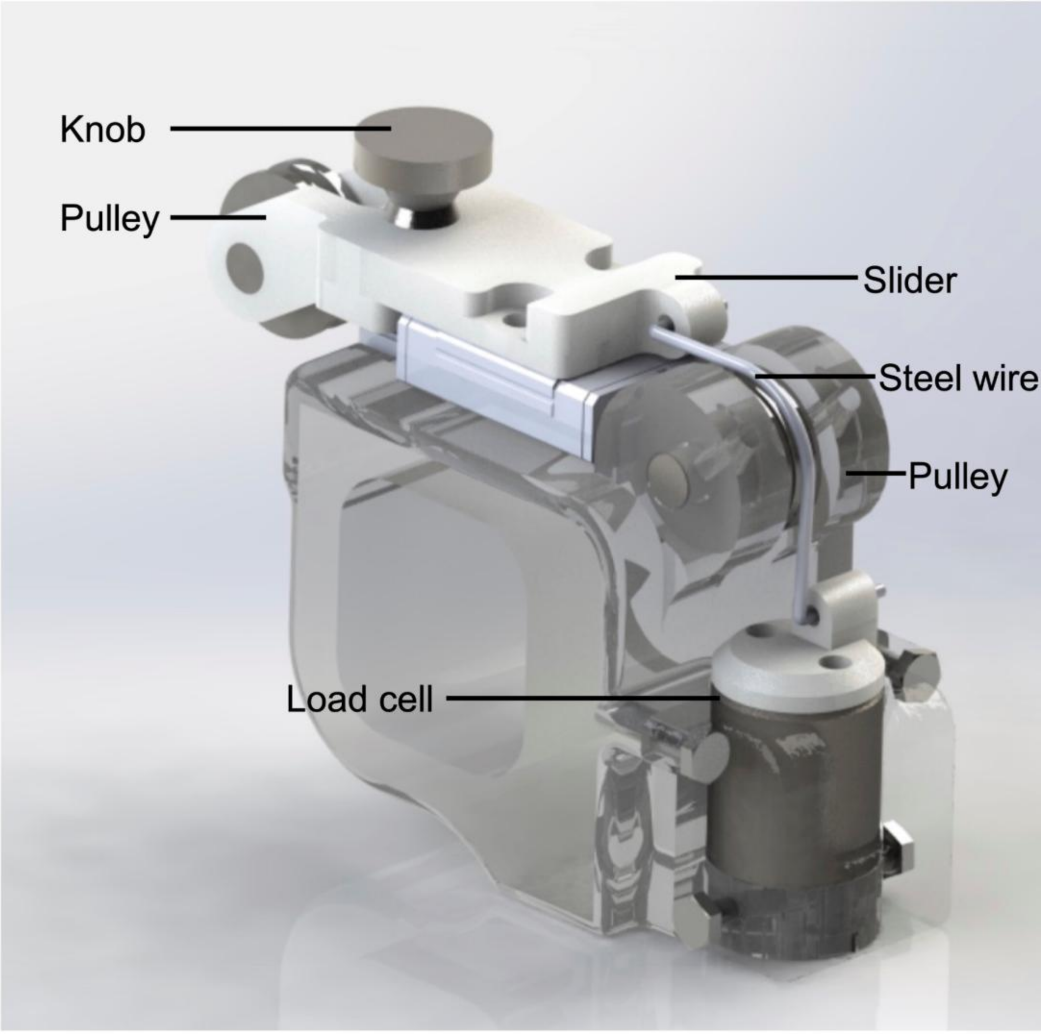

Supplementary Fig. 20: Real-time dynamometer for measuring the knot tying.

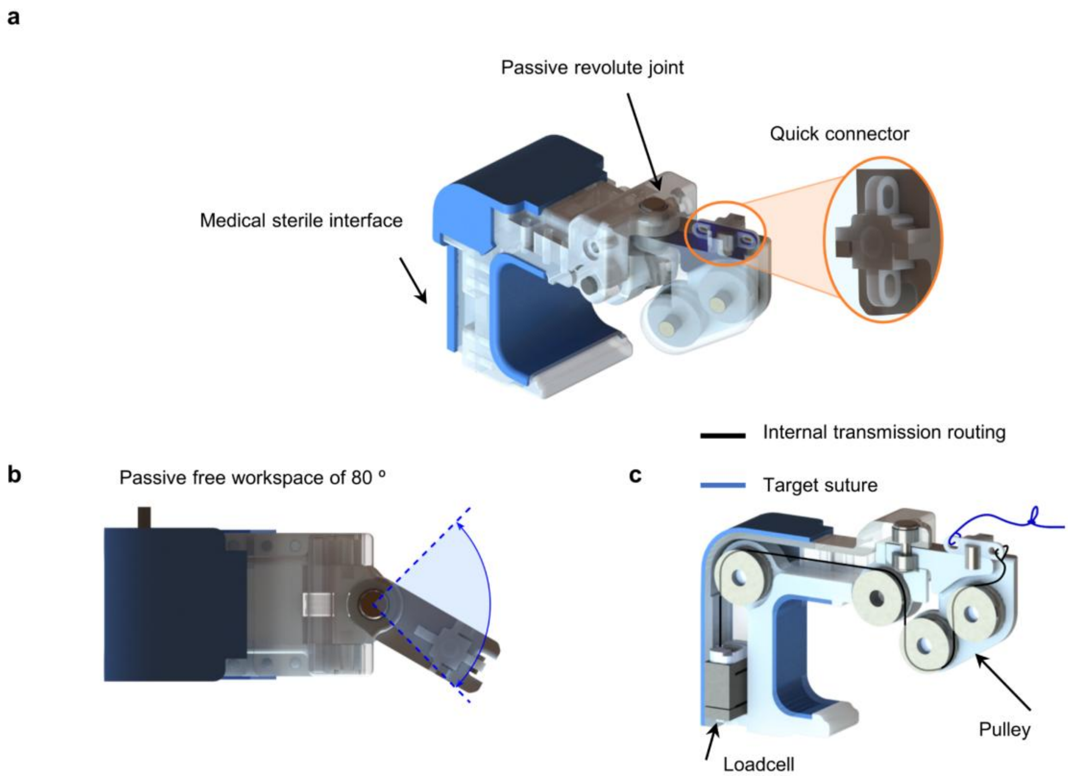

Supplementary Fig. 21: Bimanual real-time dynamometer. a, The dynamometer is mainly composed of a medical sterile interface, a passive revolute joint, and a quick connector. **b,** Passive free workspace of the passive revolute joint is 80°. **c,** The sectional view of the dynamometer.

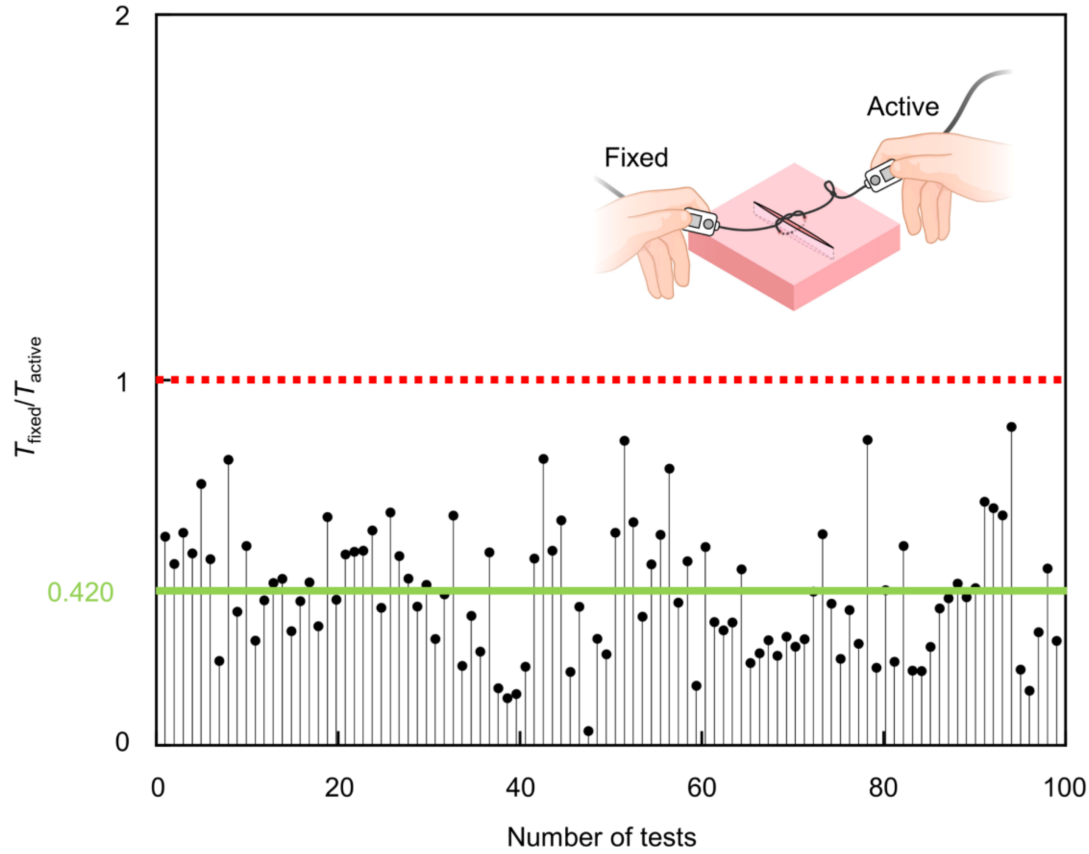

Supplementary Fig. 22: Experimental ratio of T_{fixed} to T_{active} across 100 tests. F_{peak} is reported as mean and data points (n = 100; independent experiments).

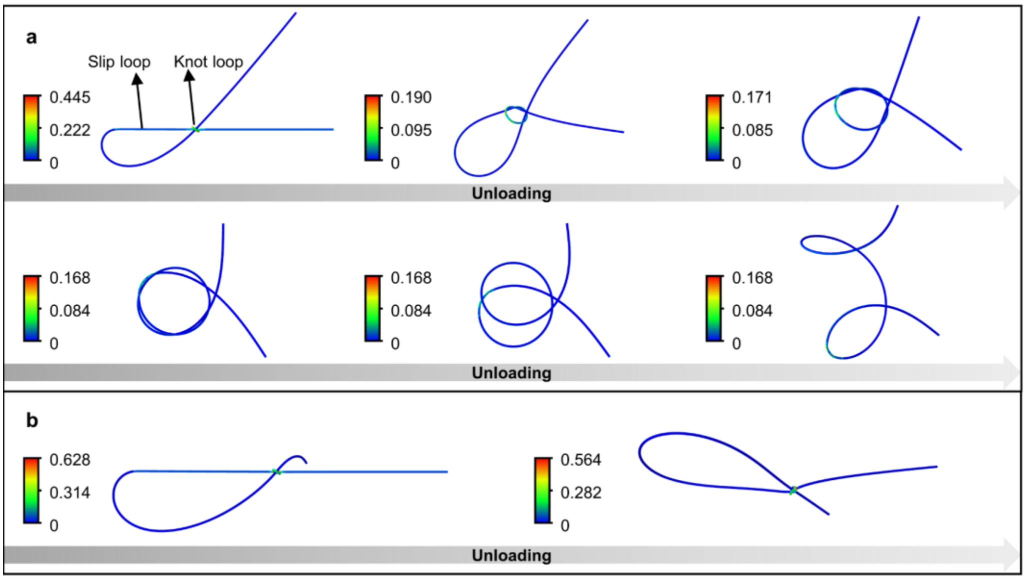

Supplementary Fig. 23: Effect of material plasticity on slipknot mechanics in FEM. **a,** Simulation of tying a slipknot with pure elastic material. When the tying force F_{tying} is released, the knot loop relaxes and gradually expands, the knot is opened when the knot loop exceeds the slip loop. **b,** Simulation of tying a slipknot with elastic-plastic material. The knot loop of the slipknot remains tightened after the release of F_{tying}. The color bars denote max principal strain.

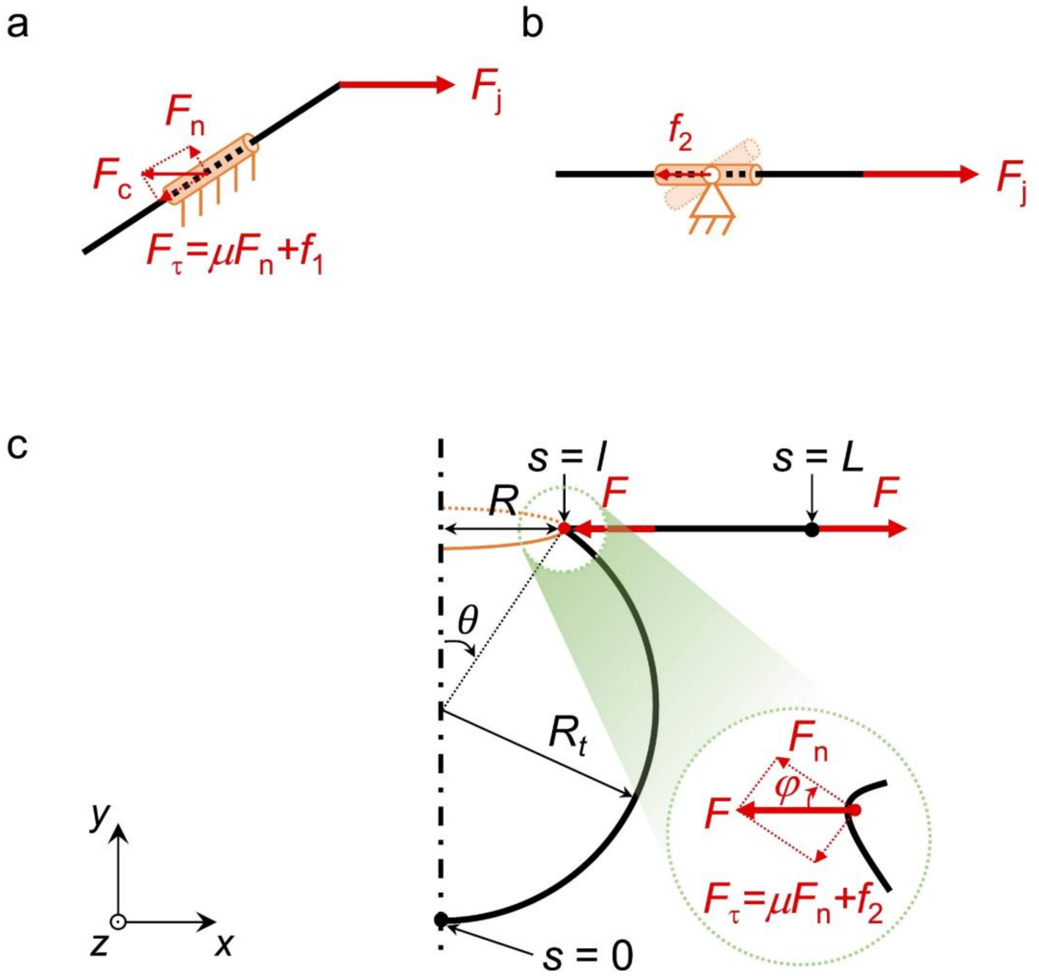

Supplementary Fig. 24: Schematic diagrams of the far-end boundary conditions and the simplified model. a, The far-end boundary condition of Stage 1**. b**, The far-end boundary condition of Stage 2. **c**, Schematic diagram of the simplified theoretical model.

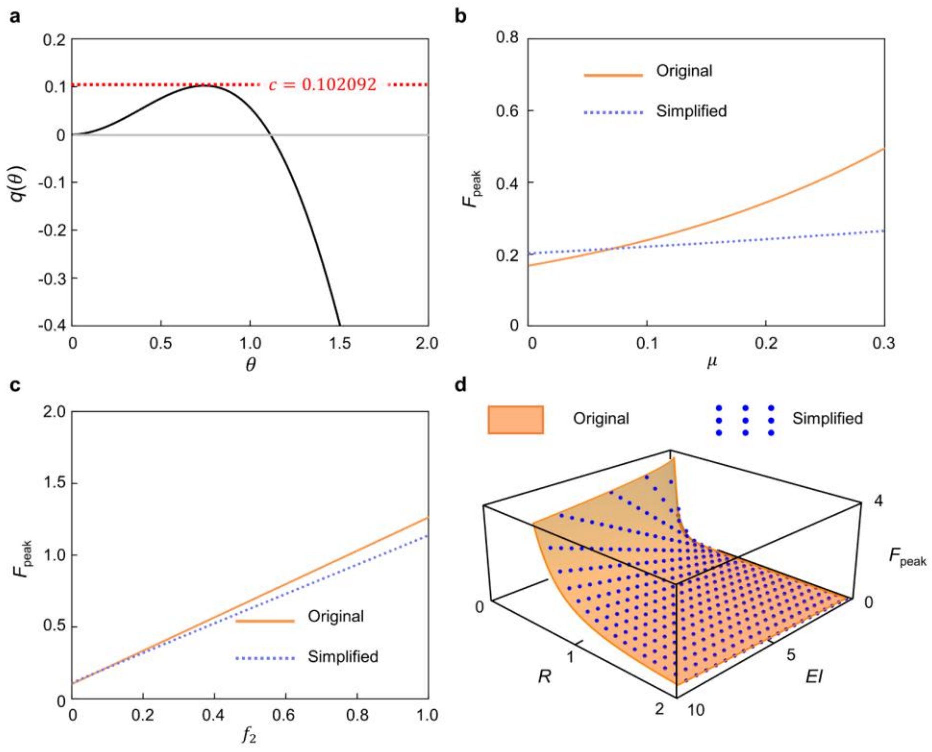

Supplementary Fig. 25: Parametric analysis of the simplified model. a, Diagram of the function $q(\theta)$, with the constant c = 0.102092 indicated by the red dotted line. **b**, Comparison between the original model (solid orange line) and the simplified model (dashed blue line) as the parameter μ varies. **c**, Comparison between the original model (solid orange line) and the simplified model (dashed blue line) as the parameter f_2 varies. **d**, 3D plots showing the relationship between F_{peak}, R and EI, comparing the original model (orange surface) with the simplified model (blue dots).

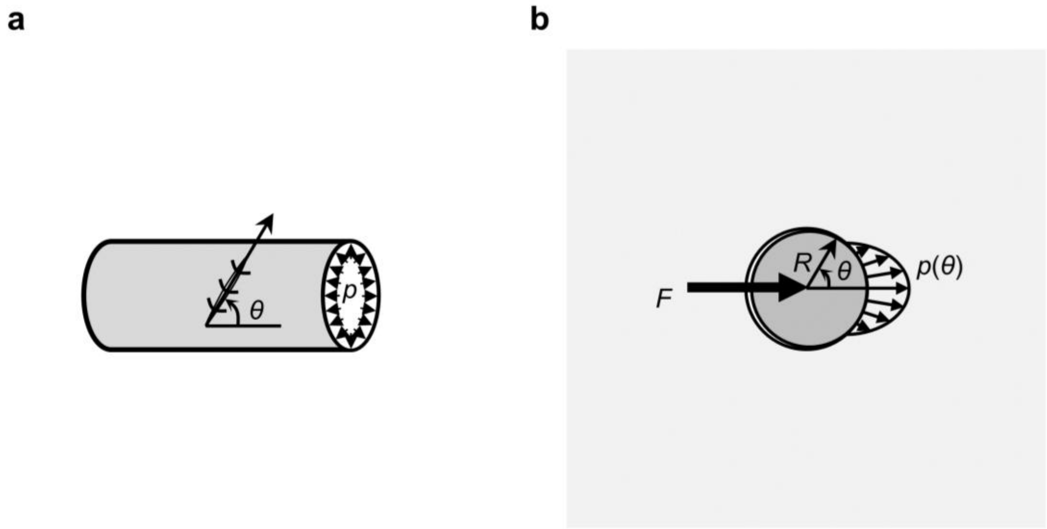

Supplementary Fig. 26: Theoretical models illustrating the feasible force range. a, Thin-walled cylinder model for the lower tension limit. **b,** Suture-tissue contact model for the upper tension limit.

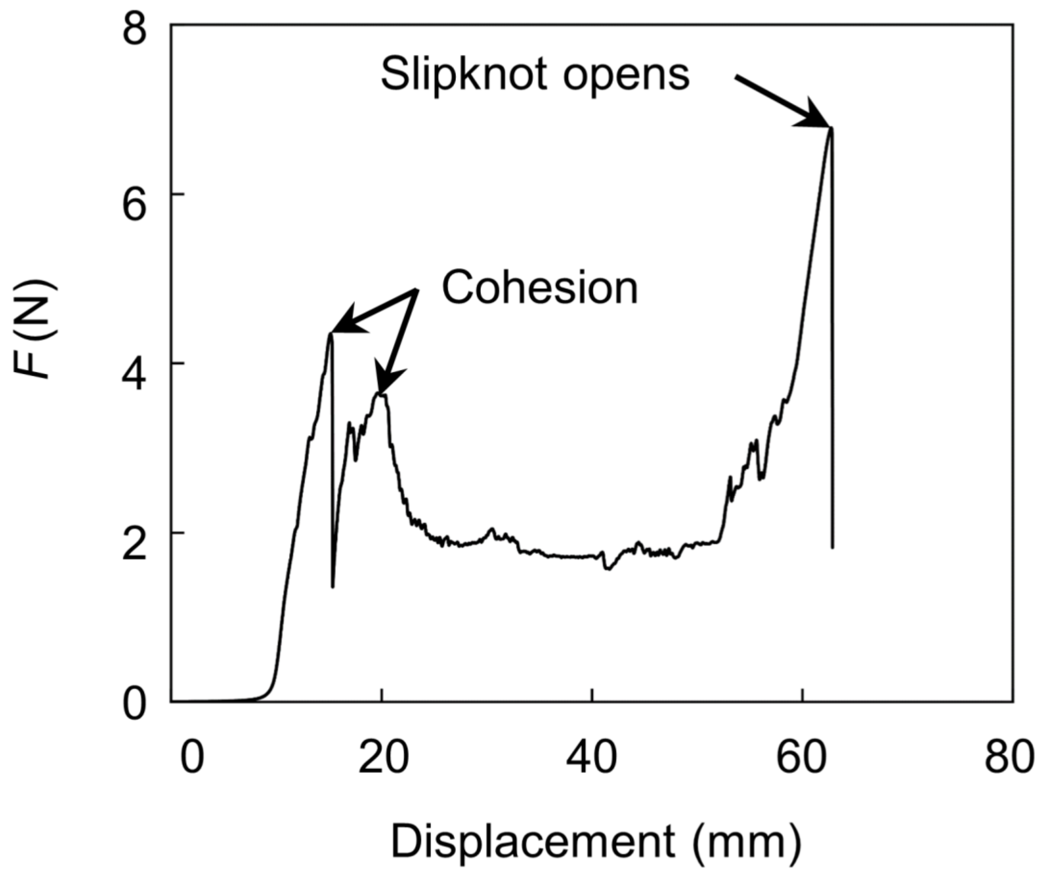

Supplementary Fig. 27: The typical force-displacement curve of a filament with cohesion. When adhesives (Scotch permanent glue stick, 6015, 3M) are applied on the slipknot to enhance the cohesion strength, several force peaks are detected at the start. Sliding occurs prior to the sliputure release, and we discovered several peak forces prior to the F_{peak} in the force-displacement curve, which attributes to the cohesion within the filament. The small peak forces can be obtained as follows: $F_{max} = \tau w L$, $\tau = \sqrt{2\mu G/h}$, where τ is defined as the interface shear strength, w and L are the width and length of the area of adhesion, μ and h are the shear modulus and thickness of the filament, G is the energy release rate.

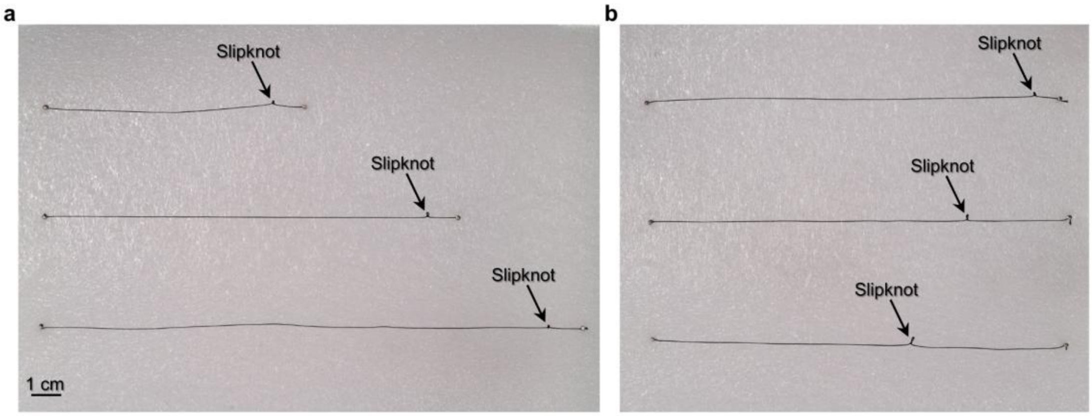

Supplementary Fig. 28: The adaptive sliputures strategy. a, Sliputures with adjustable suture lengths of 10 cm, 15 cm, and 20 cm. **b**, Sliputures with repositioned slipknots. Scale bar, 1 cm.

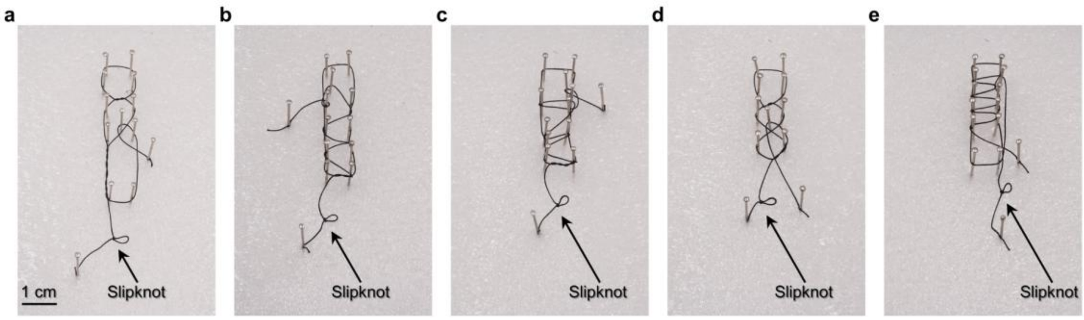

Supplementary Fig. 29: Five sliding knots fabricated with engineered slipknots. a, Tayside knot with a slipknot. **b**, Roeder knot with a slipknot. **c**, Melzer knot with a slipknot. **d**, Cross square knot with a slipknot. **e**, Blood knot knot with a slipknot. Scale bar, 1 cm.

Supplementary Videos

Video 1. High-speed dynamics of slipknot.

Video 2. Slipknot tying, tightening, and opening in FEM.

Video 3. Measuring the incision pressure on a silicone practice model.

Video 4. Exploring feasible force ranges for ex vivo colonic defect repair in a rat model.

Video 5. Validation of sliputure on an *ex vivo* rat colonic defects model.

Video 6. Validation of sliputure on an *in vivo* rat colonic defects model.

Video 7. Application of sliputure in laparoscopic surgery for colonic defect repair in a live porcine.

Video 8. Measuring the incision pressure in laparoscopic surgery.

Video 9. Application of sliputure in robotic surgery for colonic defect repair in a live porcine.

Video 10. Measuring the incision pressure in robotic surgery.

Video 11. Validation of the vision-based automatic-braking experiment in the silicone practice model.

Video 12. Validation of the vision-based automatic-braking experiment in an in vivo porcine model.

Video 13. Sliputure-assisted intelligent operation without human intervention.

Video 14. Automatic slipknot fabrication system.

Video 15. Force-displacement curve for opening DNA with a slipknot.

Video 16. Slipknot-integrated tendon-driven robotic arm enhancing human-robot interaction safety.

Supplementary Tables

Table 1 Comparison of sliputure versus force-limiting devices.

Device type	Breakaway coupling	Friction clutch	Belleville washer	Mechanical fuse	Shear pin	Sliputure
Operating principle	Predesigned weak point fractures upon overload	Friction surfaces slip beyond preset torque	Conical spring deforms elastically under load	Fractures or deforms irreversibly at overload	Shears at predetermined torque or force	Slipknot releases at peak force
Overload response	Irreversible disconnection	Reversible slipping	Elastic displacement; Non-destructive	Irreversible failure	Instantaneous irreversible failure	Slipping with dual visual and mechanical cue
MIS trocar compatibility (5-12 mm)	Bulky; Rigid; Metallic	Mechanically complex; Non-flexible	Requires rigid support; Metallic	Difficult to miniaturize	Rigid; Space-occupying	Fully flexible; Trocar-compatible
Reusability	Single-use; Requires replacement	Slips and resumes functionality	Restores elastically	Single-use; Permanent deformation	Breaks permanently; Requires replacement	Multiple-use; Reloadable with F_{tying}
Residue	Broken components may remain	Risk of particulate debris	Potential fatigue fractures	Requires fragment removal	Leaves metallic debris	No debris; Native suture remains *in situ*
Imaging compatibility (MRI/CT)	Metallic housing artifacts	Metallic components disrupt imaging	Spring-metals artifacts	Metallic components interfere	Imaging artifacts	Completely artifact-free; Non-metallic
Cost & single-use suitability	Precision parts; Relatively expensive	High manufacturing complexity	Costly to mass-produce	Economical	Simple; Easily replaceable	Compatible with standard suture production; Negligible cost
Hardware or assembly requirement	Mechanical connectors required	Motor or drive integration required	Aligned preload assembly required	Fixture and housing required	Mechanical interface required	No additional hardware or assembly required
Biocompatibility	Industrial-grade metals; Inflammation or rejection risk	External-use; Non-biocompatible;	Non-implantable Metal; Tissue reaction	Non-implantable materials typically	Sharp fracture ends; Irritation risk	Fully biocompatible; Identical to surgical suture materials

MIS, Minimally invasive surgery; MRI, Magnetic resonance imaging; CT, Computed tomography.

We considered several strategies that might be applied to limit the tension of sutures. For example, breakaway couplings incorporate deliberate weak points that snap apart at a preset axial load, isolating piping or hose lines during accidental tension and averting leaks or catastrophic spills. Other structures include friction clutch, Belleville washer, mechanical fuse, and shear pin may also work. However, in minimally invasive surgery (MIS), a force-limiting element must meet the following requirements: 1) it must fit through 5-12 mm trocars without rigid components; 2) it must deliver a highly reproducible trigger load in confined space; 3) it must leave no hazardous residue in vivo; 4) it must remain economically viable as a single-use consumable. The sacrificial structures fall short on one or more of these counts. We summarize a table (**Supplementary Table 1**) to compare those structures with the sliputure. Sliputures feature simplicity, high precision, low-cost, and residue-free.

Table 2: Parameters of PTFE monofilament sliputures in silicone oil and dry condition.

Condition	E (GPa)	d (mm)	μ	f_2 (F_{tying} = 2.500 N)	f_2 (F_{tying} = 5.000 N)	f_2 (F_{tying} = 7.500 N)	f_2 (F_{tying} = 10.000 N)
Dry	2.700	0.235	0.165	0.543	1.649	2.862	3.900
Silicone oil	2.700	0.235	0.119	0.547	1.380	2.666	3.393

Table 3: Parameters of Mersilk sliputures in silicone oil, synthetic blood, and dry condition.

Condition	E (GPa)	d (mm)	μ	f_2 (F_{tying} = 0.400 N)	f_2 (F_{tying} = 0.800 N)	f_2 (F_{tying} = 1.600 N)	f_2 (F_{tying} = 3.200 N)
Dry	9.745	0.150	0.145	0.246	0.442	0.713	0.763
Silicone oil	9.745	0.150	0.119	0.065	0.233	0.374	0.548
Synthetic blood	9.745	0.150	0.260	0.328	0.622	1.104	1.125

Table 4: Parameters of Vicryl sliputures in silicone oil and dry condition.

Condition	E (GPa)	d (mm)	μ	f_2 (F_{tying} = 1.600 N)	f_2 (F_{tying} = 3.200 N)
Dry	14.668	0.150	0.157	0.551	0.611
Silicone oil	14.668	0.150	0.180	0.521	0.591

Table 5: The comparison of F_{peak} of PTFE monofilament sliputures in silicone oil and dry condition.

F_{tying} (N)	Exp.- dry (N)	Exp.- liquid (N)	Theory-dry (N)	Theory-liquid (N)
2.500	1.766	1.439	1.970	1.646
5.000	4.104	3.548	3.371	2.655
7.500	5.826	5.563	4.864	4.179
10.000	7.388	6.763	6.115	5.026

Table 6: The comparison of F_{peak} of Mersilk sliputures in silicone oil and dry condition.

F_{tying} (N)	Exp.-dry (N)	Exp.-liquid (N)	Theory-dry (N)	Theory-liquid (N)
0.400	1.517	0.756	1.978	1.516
0.800	2.142	1.633	2.226	1.721
1.600	2.368	2.135	2.568	1.894
3.200	2.414	2.295	2.631	2.107

Table 7: The comparison of F_{peak} of Mersilk sliputures in synthetic blood and dry condition.

F_{tying} (N)	Exp.-dry (N)	Exp.-liquid (N)	Theory-dry (N)	Theory-liquid (N)
0.400	1.517	1.979	1.978	3.538
0.800	2.142	2.223	2.226	3.962
1.600	2.368	2.571	2.568	4.647

3.200	2.414	2.540	2.631	4.677

Table 8: The comparison of F_{peak} of Vicryl sliputures in silicone oil and dry condition.

F_{tying} (N)	Exp.- dry (N)	Exp.- liquid (N)	Theory-dry (N)	Theory-liquid (N)
1.600	3.316	3.647	3.391	3.733
3.200	3.383	3.829	3.468	3.826